Vol.48 No.4　2024

Journal

TOEI

TPM-2-08s25

H'cJの3σ/Ave. 0.2%※1 を実現
渦電流補正方法※2 も確立済

試料測定磁界	最大試料直径
max 15 Tesla	10mm

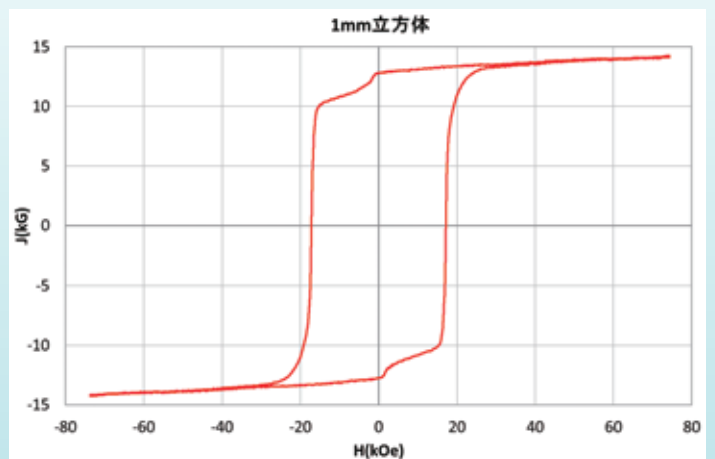### パルス励磁型磁気特性測定装置

永久磁石および磁性体粉末を固形化した高磁化試料のヒステリシス曲線の自動測定および描画、SPD（Singuler Point Detection）測定が可能です。（RT〜+200℃）

※1　電気学会資料 MAG-18-088 参照
※2　電気学会資料 MAG-07-011 参照

NdFeB（sintered）測定例
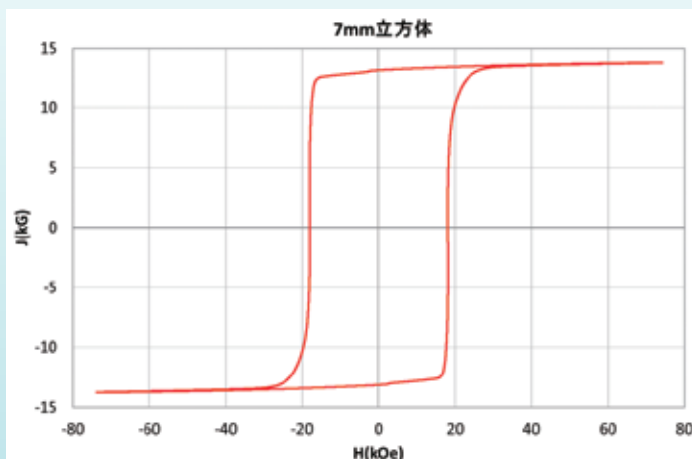
7mm立方体

1mm立方体

1mm 立方体測定用検出コイルはオプション品です

東英工業では他に振動試料型磁力計（VSM）、直流自記磁束計（JIS C2501 準拠）を始め、各種磁気測定装置を取り揃えております。ぜひお問い合わせ下さい

TOEI 東英工業株式会社

http://www.toeikogyo.co.jp

JOURNAL OF THE MAGNETICS SOCIETY OF JAPAN

Journal of the Magnetics Society of Japan
Vol. 48, No. 4

CONTENTS

<Paper>

Effect of Zr Substitution on the Nd-based Magnets: Theoretical Investigation of (Zr,Nd)(Fe,Ti)₁₂ Compounds

N. Y. Merkt, S. Erdmann, T. Klüner, H. İ. Sözen

Institute of Chemistry, Carl-von Ossietzky University of Oldenburg., *Carl-von-Ossietzky-Straße 9-11 Oldenburg D-26129, Germany*

This research aims to identify an alternative solution for the $Nd_2Fe_{14}B$ magnet in light of the scarcity of rare-earth (RE) resources. The investigation uses density functional theory (DFT) calculations to assess the effect of partial substitution of Nd with the transition metal (TM) Zr within the $ThMn_{12}$ structure, focusing specifically on the $(Zr_{0.5}Nd_{0.5})Fe_{11}Ti$ compound. In order to gain a comprehensive understanding, an investigation of intrinsic and magnetic properties, including saturation magnetization (M_S), Curie temperature (T_C) and magnetic anisotropy energy (MAE), is carried out on binary to quinary compounds $RFe_{11-y}Ti_y$ (R: Nd, Zr and $Zr_{0.5}Nd_{0.5}$, y: $0 \leq y \leq 1$) and $(Zr_{0.5}Nd_{0.5})Fe_{10}CoTi$. The substitution of Ti at different concentrations for thermodynamic stabilization is studied in ternary and quaternary compounds $RFe_{12-y}Ti_y$ ($0 \leq y \leq 1$). In addition, the influence of Co on phase stability and intrinsic magnetic properties is studied in the quinary compound $(Zr_{0.5}Nd_{0.5})Fe_{10}CoTi$. Special attention is given to the treatment of the 4f electrons of Nd and their interaction with the 3d electrons. Theoretical results are compared with available experimental data, although the limited availability of data, especially for Zr-containing compounds, limits the scope of such comparisons. From the literature and our calculations of binary and ternary compounds, we are encouraged to the quaternary and quinary calculations. Promising magnetic properties of an Nd-lean quaternary compound suitable for engineering applications have been identified. In particular, for the quaternary compound $ZrNdFe_{22}Ti_2$, calculated values of $|BH|_{max} = 525$ kJ/m³ and $T_C = 783$ K are close to those of the $Nd_2Fe_{14}B$ magnet.

Keywords: hard magnets, Nd-lean permanent magnets, alternative magnets, zirconium substitution, cobalt substitution, $ThMn_{12}$-phase

1. Introduction

In recent years, there has been an growing demand for low-cost and resource-efficient hard magnets, particularly in the renewable energy and e-mobility sectors. Currently, the most prevalent magnets are made from rare-earth (RE) and transition metal (TM) elements. The strongest is the $Nd_2Fe_{14}B$ compound developed in the early 1980s.[1,2]

The combination of RE and TM elements results in alloys with high saturation magnetization (M_S), high Curie temperature (T_C) and high magnetocrystalline anisotropy energy (MAE). The high values for M_S and T_C are attributed to the presence of the TM atoms, while RE elements are responsible for the high anisotropy. Nevertheless RE elements such as Nd, Dy, Sm and Tb, as well as some TM elements such as Co are considered critical for future applications.[2–4] In addition, there is a global monopoly of RE elements, which necessitates the search for RE-lean or RE-free hard magnetic materials.[5,6]

Several methods for developing RE-lean magnets have been documented in the literature. For instance, grain size reduction is used to achieve a higher coercive field strength and the critical element Dy can be omitted.[7,8] The coercivity can be significantly increased by applying the grain boundary diffusion process, which leads to the reduction of critical RE elements such as Dy or Tb.[9,10] In addition, the partial replacement of the critical RE elements with more abundant and low-cost elements has

been explored (*e.g.* see Sakuma *et al.*[11]). So far, this process has mainly been used to produce magnets for low to medium temperature applications.

We focus on the physical and magnetic properties of RE-lean permanent magnets based on the $ThMn_{12}$ prototype structure (also referred to as the 1:12 phase in this paper). It is worth noting noted that the 1:12 (RE:Fe) phase has a lower RE content than $Nd_2Fe_{14}B$ and exhibits promising magnetic properties.[12–14] In our previous research we investigated the abundant and inexpensive elements Y and Ce as potential substitutes for the critical element Nd and their effect on the magnetic properties and thermodynamic phase stabilities of the 1:12 phase.[15,16]

In this paper, we consider Zr as a promising replacement for the RE element Nd. Substituting Zr for Nd can result in more cost-effective and sustainable magnets, as Zr is more abundant and affordable than Nd.[17,18] Previous studies have reported on the phase stability of compounds with Zr substitution in the 1:12 phase.[11,19,20] The studies demonstrated that replacing Nd with Zr has the potential to generate a saturation polarization similar to or greater than that of $Nd_2Fe_{14}B$, as well as an anisotropy field comparable to it.[20] Furthermore, it should be noted that Zr exclusively substitutes on the 2a sites of the 1:12 phase that are already occupied by RE elements. Nevertheless, the main experimental challenge lies in the substitution of Zr in

Corresponding author: N. Y. Merkt
(nico.yannik.merkt@uni-oldenburg.de)

these 2a sites, which forms a solid solution with Fe, and compounds with a Zr concentration of up to 30% have been produced so far.[21] A possible solution to this problem is the selective laser melting method used by Neznakhin *et al.*[22], as it has successfully produced the compound (Zr,Sm)Fe$_{11}$Ti with a 1:1 ratio of Zr to RE. Based on the selective laser melting method[22] and our theoretical calculations given in the Sec. 3.1, the concentration of 50% is considered.

In order to have a systematic understanding of the intrinsic magnetic properties of Zr-substituted 1:12 compounds, we have started with the binaries and ternaries of M$_2$Fe$_{24-y}$Ti$_y$ alloys (where M = Zr and Nd and y: $0 \le y \le 2$). Since the 1:12 binary phases are not thermodynamically stable, Ti was used as a stabilizer.[23–26] The Zr substitution and Ti solubility in the quaternary compounds (Zr,Nd)Fe$_{24-y}$Ti$_y$ were studied. Once the equilibrium Ti concentration was found, Co was additionally considered as a quinary substitution to study its effect on magnetic properties and stabilities.

The paper is structured as follows: In Sec. 2, the computational details of the theoretical approaches are explained. Then, in Sec. 3 ab initio based intrinsic magnetic properties are given. We have started with the solution enthalpies and formation energies of the considered compounds in Sec. 3.1. Physical properties such as lattice constants and cell volumes are discussed. In Sec. 3.2 the magnetic properties are given, starting with the total magnetic moment and the magnetization. The calculated $|BH|_{max}$ values are presented in Sec. 3.3. Another important intrinsic magnetic property, the Curie temperature, is calculated using the Korringa-Kohn-Rostoker (KKR) method and is discussed in Sec. 3.4. The last magnetic property calculated in this paper, the magnetocrystalline anisotropy energy (MAE), is given in Sec. 3.5. Finally, we conclude the paper with remarks and discussions in Sec. 4.

2. Computational Details

All theoretical calculations were performed by spin-polarized density functional theory (DFT) using the Vienna *ab-initio* Simulation Package (VASP).[27,28] The projector-augmented wave (PAW) method was used as implemented in VASP. The exchange correlation effects were treated within the Perdew-Burke-Ernzerhof (PBE)[29] generalized Gradient Approximation (GGA). For the magnetocrystalline anisotropy energy the local spin density approximation (LSDA)[30] was considered in addition to the GGA. Optimized structures from GGA were used in these MAE calculations.

To scan the Brillouin zone we used a Γ-centred k-point grid of 12×12×10 meshes for the 26-atom supercells used. The cut-off energy of the plane wave basis was set to 500 eV and the smearing parameter to 0.1 eV. The convergence criteria within the self-consistent field scheme was set to 10^{-5} eV for all calculations except the anisotropy calculations where the criteria was set to 10^{-7} eV. The choice of input parameters gives energy convergence within an error of less than 1 meV/atom.

The 4f electrons of Nd have been treated carefully, although this is a challenge in DFT. The f electrons of Nd have been considered in the in-core state, which gives good mechanical and elastic properties.[31] To calculate the magnetic properties, we went beyond DFT and performed a DFT+U treatment using the Dudarev method[32] with a Hubbard correction of U = 6 eV. This Hubbard correction term has been used previously in the literature for 1:12 Nd-based compounds with good results.[15,16,33]

Treating the 4f electrons in the in-core state, hybridization with other orbitals is completely neglected and instead atomic physics is applied to the Nd-4f states. Note that only the spin magnetic moment is calculated from the self-consistent DFT calculations. To obtain the total magnetic moment, the orbital magnetic moment must be added. The orbital magnetic moment is made up of $g_j \cdot J$ where g_j is the Landé g-factor (g_{Nd} = 8/11 [34]) and J is the total angular momentum of 9/2. The total angular momentum results from Hund's first rule and the full spin polarization (S = 3/2) of the three 4f electrons of the element Nd. The orbital magnetic moment of Nd can be estimated to be 3.273 μ_B, using the equation $J = |L-S|$ (for elements with less than half a full f shell) with L = 6. In case of the GGA+U calculations, the calculated spin fraction of the Nd-4f electrons and the value of $g_j \cdot J$ were added to avoid double counting for the spin fraction of the 4f electrons.

A collinear self-consistent calculation was performed to calculate the magnetocrystalline anisotropy. The resulting relaxed structures from the GGA calculations were used as input for the non-collinear calculations, which take into account the spin-orbit coupling. For each non-collinear run, the magnetic moment was aligned with one of the crystallographic directions [001], [010] and [100].

For the Curie temperature (T_C), the Liechtenstein method[35] was used to determine the exchange interaction energies J_{ij} for the ferromagnetic (FM) and local moment disorder (LMD) states of the 1:12 phase. This was achieved by applying the GGA via the Korringa-Kohn-Rostoker (KKR)[36,37] Green's function method as implemented in the AkaiKKR[38] code, also known as MACHIKANEYAMA. This method implements the atomic sphere approximation (ASA) using the coherent potential approximation (CPA).[39,40] Continuous concentration changes of both RE and TM sublattices were considered based on the CPA. Moruzzi, Janak and Williams (MJW)[41] parameterized the local density approximation (LDA)[42,43] which is the basis for all KKR calculations. In this study the scattering of the system is considered up to d-scattering (l_{max} = 2), *i.e.* the f electrons are placed in the valence state on the basis of the open core approximation.[34,44] The corresponding results of the GGA-PBE relaxation calculations are used as structural input for the T_C calculations.
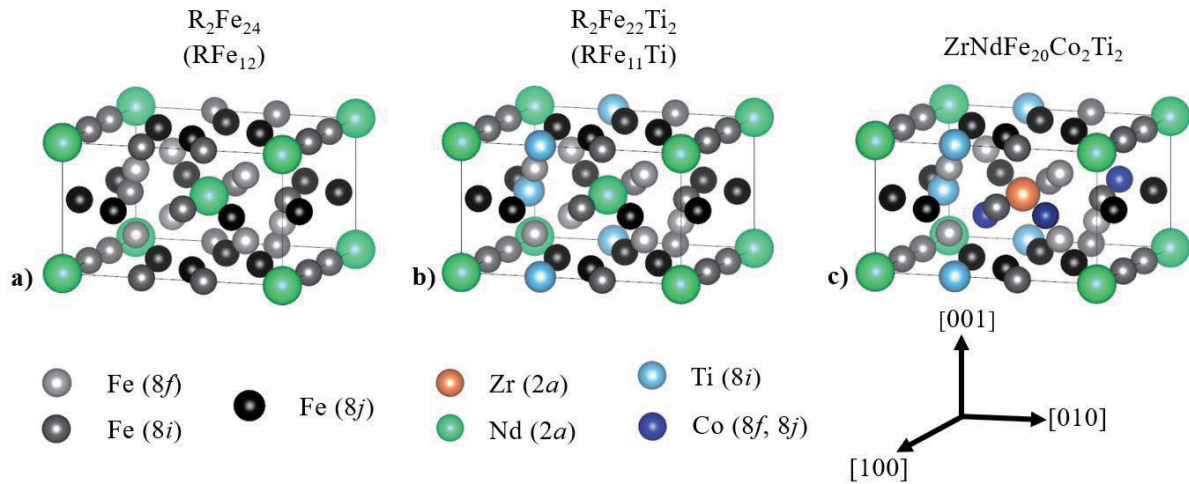
Fig. 1 Schematic representation of the 2 formula unit (f.u.) (26 atoms) body-center-tetragonal ThMn$_{12}$ (I4/mmm, space group number 139) 1:12 phases. (a) Unstable RFe$_{12}$, (b) 2 Ti atom substituted (7.7 at. %) R$_2$Fe$_{22}$Ti$_2$ (RFe$_{11}$Ti) and (c) 2 Ti and 2 Co substituted (each 7.7 at. %) supercell RFe$_{10}$CoTi (R$_2$Fe$_{20}$Co$_2$Ti$_2$). Ti atoms are substituted in energetically favorable 8i sites and Co atoms are substituted in energetically favorable 8f and 8j sites.

3. Results and Discussion

3.1 Stability of Ti, Co and Zr substituted 1:12 compounds

Besides the well known Nd$_2$Fe$_{14}$B magnet[45,46], another class of typical compounds that fulfil the technological requirements for hard magnetic applications is in the form of RFe$_{12-y}$Ti$_y$. Figure 1(a) shows a schematic representation of the RFe$_{12}$ compound.

RFe$_{12}$ compounds are known to be thermodynamically unstable.[23–26] To stabilize a bulk system with the ThMn$_{12}$ structure, partial substitution of Fe atoms is required. Ti is a commonly used and typical stabilizing element[13,47], and is therefore used. The effect of Co substitution on both the stabilization and the magnetic properties is studied. In addition to these substitutions on the TM site, we have investigated Zr substitution on the RE site to make the Nd concentration lean.

Primarily, the phase formation energies of the ternary phases with X substitution (X = Ti and Co) are considered:

$$E^f = \left(Nd_2Fe_{24-y}X_y\right) - 2\mu_{Nd} - (24 - y)\mu_{Fe} - y\mu_X$$
$$= 2E^f(NdFe_{12}) + E^{sol}(y) \tag{1}$$

$E(Nd_2Fe_{24-y}X_y)$ is the total energy of the X substituted 1:12 phase. X can be Ti or Co on the TM sublattice. For a given Ti and Co concentration all possible configurations have been investigated and the most energetically favorable configuration is taken into account in this formula. Note that a similar formulation can also be written for Zr substitution on the RE site. μ represents the ground state of the considered elements. In case of μ_{Fe} this is the body centred cubic (bcc) and ferromagnetic (FM) structure. For the elements Co (μ_{Co}), Ti (μ_{Ti}), Nd (μ_{Nd}) and Zr (μ_{Zr}) the hexagonal structure (hcp) or, in the case of Nd, the double-hexagonal close-packed structure (dhcp) has been considered. The elements Ti, Nd and Zr are treated as nonmagnetic (NM) and Co in the FM state.

The phases are thermodynamically stable (unstable) for negative (positive) formation energies. Although pure unaries are considered as the reference, the results are expressed in terms of the formation energy E^f(NdFe$_{12}$) of the unstable phase NdFe$_{12}$. Various formulations can be considered instead of the base compound. However, due to the shortage of quaternary phase diagrams, natural references have been considered, which are again base compounds and unaries:

$$E^{sol}(y) = E\left(Nd_2Fe_{24-y}X_y\right) - 2E(NdFe_{12}) + y(\mu_{Fe} - \mu_{Ti}) \tag{2}$$

Since the solution enthalpy calculations include reference elements which are critical to the resulting energies, accurate modelling is required. Table 1 compares the physical and magnetic properties of the pure elements with experimental data.

According to the calculations, the Nd-based 1:12 compound, NdFe$_{12}$, is thermodynamically unstable with a formation energy of 0.94 eV, in agreement with previous reports.[23–25] However, ZrFe$_{12}$ was calculated to be stable with a formation energy of −0.76 eV, in accordance with the other theoretical work.[57] This is not the case for the 50% substitution of Nd with Zr, the compound (ZrNd)Fe$_{12}$, which has a formation energy of 0.16 eV.

As 50% substitution of Nd by Zr is apparently not sufficient to stabilize the ternary phase, additional substitution of Fe by Ti is required. For the compounds containing one Ti atom, NdFe$_{11.5}$Ti$_{0.5}$ and (ZrNd)Fe$_{11.5}$Ti$_{0.5}$, the formation energies were calculated to be −0.03 eV and −0.79 eV, respectively. Comparing

Table 1 Calculated physical and magnetic properties of the pure elements that are included in solution enthalpy formalism in Eq. 2. a and c are the lattice constants, B_0 is the bulk modulus and m_{tot} is the magnetic moment (where NM stands for nonmagnetic).

Alloy	Lattice constants (Å)		Experimental Lattice constants (Å)		Bulk modulus	Experimental Bulk modulus	Magnetic moment	Experimental Magnetic moment m_{tot}
	a	c	a	c	(GPa)	(GPa)	(μ_B/atom)	(μ_B/atom)
Fe	2.832	2.832	2.668[h 48]	2.668[h 48]	185.47	159-173[d 48]	2.21	2.22[a 49]
Co	2.489	4.036	2.5[a 50]	4.1[a 50]	212.15	199 ±6[a 50]	1.63	1.53[f 49]
Ti	4.553	2.817	4.60[a 51]	2.83[a 51]	128.93	102-119[a 51]	NM	NM[f 52]
Nd	3.704	11.935	3.658[d 53]	11.839[d 53]	33.84	25.4-34.9[d 53]	NM	NM[a 54]
Zr	3.235	5.166	3.233[b 55]	5.146[b 55]	93.57	92-102[b 55]	NM	NM[g 56]

[a]X-ray diffraction (XRD) analysis at 300 K.
[b]High-pressure (ultrasonic) measurements combined with X-ray techniques.
[c]X-ray diffraction (XRD) analysis at >573 K.
[d]With Vibrating Sample Magnetometer at 300 K.
[e]Neutron Diffraction at 300 K.
[f]By measuring the flux change.

these energies, it can be seen that in case of the Zr-substituted alloy, the substitution of one Ti atom is sufficient to stabilize the compound. In case of the ternary compound without Zr, the energy of formation is just below 0 eV. As Zr has the potential to reduce the Ti concentration, the magnetic properties are enhanced.

The effect of Ti stabilization has been studied for the $ZrNdFe_{24-y}Ti_y$ compounds as given in Fig. 2. It starts with the substitution of the first Ti atom in each TM site, *i.e.* $8i$, $8j$ and $8f$, in the supercell consisting of 26 atoms (2 formula units (f.u.)). Note that a single Ti atom corresponds to 3.8 at. %. As in previous work for Ce and Nd-based 1:12 compounds[15,58], the $8i$ site is calculated to be the most energetically favorable site. The solution enthalpies for the $8j$ and $8f$ sites are higher by 0.53 and 0.72 eV, respectively. Therefore, only the $8i$ sublattice was considered for the substitution of the remaining Ti atoms.
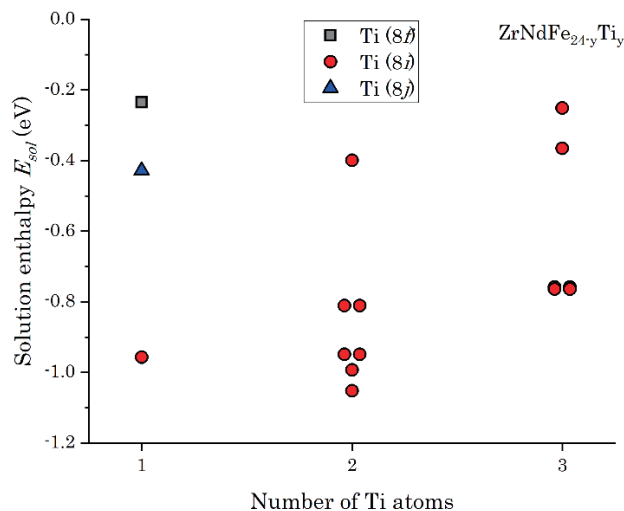

Fig. 2 Calculated Ti solution enthalpies for $(ZrNd)Fe_{24-y}Ti_y$ according to Eq. 2. The first Ti atom is considered in $8i$, $8j$ and $8f$ sites one by one. Then the remaining Ti atoms are substituted on $8i$ site due to the lower solution enthalpy and all possible configurations are considered.

Note that the exclusion of the $8j$ and $8f$ sublattices is also supported by experimental work.[59,60] The origin of the $8i$ preference is due to the larger Wigner-Seitz radius of this site compared to the $8f$ and $8j$ sites.[61] In case of substitution of the second and third Ti atom, all possible configurations on $8i$ sites were considered. The Ti solubility studies on $(ZrNd)Fe_{24-y}Ti_y$ give an equilibrium Ti concentration of 7.7 at. %, which is the same as in case of $NdFe_{12-x}Ti_x$ and $CeFe_{12-x}Ti_x$.[15,16,58,62] The corresponding structure is shown in Fig. 1(b).

Although Ti stabilizes the Zr substituted 1:12 compounds, it reduces the overall magnetic moment due to its nonmagnetic (NM) nature. For instance, $(ZrNd)Fe_{22}Ti_2$ has 4.06 μ_B/f.u. less total magnetic moment than the Ti-free 1:12 compound. Therefore, ferromagnetic (FM) Co was considered as another substitutional element for $(ZrNd)Fe_{24-x}Co_x$ and $(ZrNd)Fe_{22-x}Ti_2Co_x$ to improve the magnetic properties and to understand its effect on the stability.

Figures 3 and 4 show the site preference of Co substitutions and equilibrium concentrations for the considered 1:12 compounds. As shown, Co prefers to substitute at $8f$ and $8j$ sites for both $(ZrNd)Fe_{24-x}Co_x$ and $(ZrNd)Fe_{22-x}Ti_2Co_x$ cases. In case of the $(ZrNd)Fe_{24-x}Co_x$ compounds it can be seen in Fig. 3 that the first Co atom is substituted into the $8f$ site with the solution enthalpy of -0.22 eV. This is followed by the $8j$ and $8i$ sites with -0.21 eV and -0.18 eV, respectively. After keeping the first Co atom in the $8f$ position and replacing the second Co atom, the lowest energies of the $8j$, $8f$ and $8i$ sites are obtained with -0.24 eV, -0.22 eV and -0.17 eV, respectively. As the equilibrium concentration is at 2 Co atoms (7.7 at. %), additional Co atoms lead to higher solution enthalpies. It is also noticeable that the $8j$ site gives the most negative energy for the third Co atom and from the fourth to the sixth Co atom the $8f$ site gives the lowest energies.

As can be seen in Fig. 4 in case of the $(ZrNd)Fe_{22-x}Ti_2Co_x$ compounds, again the substitution of Co into the $8f$ site with the solution enthalpy of -0.16 eV, followed by $8j$ and $8i$ with about -0.14 eV, leads to the most stabilized compound. For the second Co atom the $8j$ site yield the lowest solution enthalpy with -0.22 eV, followed by $8f$ with -0.19 eV and $8i$ with -0.18 eV. For the third to sixth Co atoms, the $8j$ sublattice is the energetically most favorable site. Since sublattice $8i$ has

Table 2 GGA calculated physical and magnetic properties of the most stable Co containing compounds (see Figs. 3 and 4) starting from $ZrNdFe_{24}$ and $ZrNdFe_{22}Ti_2$ with increasing Co content.

Alloy	Lattice constants (Å)			Cell volume	Spin magnetic moment at 2a site m^{2a}_{tot}	Total magnetic moment m_{tot}	Saturation magnetization $\mu_0 M_S$	Maximum energy product $\|BH\|_{max}$
	a	b	c	(Å³)	(μ_B/f.u.)	(μ_B/f.u.)	(T)	(kJ/m³)
$ZrNdFe_{24}$	8.419	8.419	4.656	165.01	-0.50 (m_{Zr}^{2a}) -0.26 (m_{Nd}^{2a})	27.16	1.92	732.20
$ZrNdFe_{23}Co$	8.419	8.419	4.659	165.15	-0.50 (m_{Zr}^{2a}) -0.26 (m_{Nd}^{2a})	27.34	1.93	740.30
$ZrNdFe_{22}Co_2$	8.407	8.423	4.664	165.13	-0.50 (m_{Zr}^{2a}) -0.26 (m_{Nd}^{2a})	27.34	1.93	740.97
$ZrNdFe_{21}Co_3$	8.417	8.417	4.665	165.24	-0.50 (m_{Zr}^{2a}) -0.26 (m_{Nd}^{2a})	27.46	1.94	745.95
$ZrNdFe_{20}Co_4$	8.419	8.417	4.672	165.55	-0.50 (m_{Zr}^{2a}) -0.26 (m_{Nd}^{2a})	27.70	1.95	756.67
$ZrNdFe_{19}Co_5$	8.417	8.417	4.682	165.83	-0.51 (m_{Zr}^{2a}) -0.26 (m_{Nd}^{2a})	27.95	1.96	767.69
$ZrNdFe_{18}Co_6$	8.410	8.410	4.691	165.91	-0.50 (m_{Zr}^{2a}) -0.26 (m_{Nd}^{2a})	28.02	1.97	770.45
$ZrNdFe_{22}Ti_2$	8.411	8.497	4.704	168.08	-0.49 (m_{Zr}^{2a}) -0.27 (m_{Nd}^{2a})	23.10	1.60	510.17
$ZrNdFe_{21}CoTi_2$	8.408	8.495	4.708	168.13	-0.49 (m_{Zr}^{2a}) -0.26 (m_{Nd}^{2a})	23.19	1.61	513.86
$ZrNdFe_{20}Co_2Ti_2$	8.391	8.492	4.719	168.11	-0.49 (m_{Zr}^{2a}) -0.26 (m_{Nd}^{2a})	23.22	1.61	515.62
$ZrNdFe_{19}Co_3Ti_2$	8.407	8.481	4.715	168.11	-0.49 (m_{Zr}^{2a}) -0.26 (m_{Nd}^{2a})	23.14	1.60	511.78
$ZrNdFe_{18}Co_4Ti_2$	8.399	8.469	4.719	167.84	-0.48 (m_{Zr}^{2a}) -0.26 (m_{Nd}^{2a})	22.95	1.59	505.11
$ZrNdFe_{17}Co_5Ti_2$	8.402	8.459	4.707	167.28	-0.47 (m_{Zr}^{2a}) -0.25 (m_{Nd}^{2a})	22.54	1.57	490.70
$ZrNdFe_{16}Co_6Ti_2$	8.407	8.449	4.698	166.84	-0.47 (m_{Zr}^{2a}) -0.25 (m_{Nd}^{2a})	22.17	1.55	477.03

a larger Wigner-Seitz radius, the preference for Co in sublattices 8f and 8j is suspected to produce the more stable crystal structures. The theoretically calculated site preference is in agreement with experimental reports[11,19,63], which reported that Co prefers the 8f and 8j sites. In addition, for both series of compounds, a trend is observed that the 8i site generally has higher solution enthalpies and the 8j and 8f sites are more stable. The Co equilibrium concentration of 7.7 at. % was calculated for both compounds. The schematic representation of the most stable quinary phase is shown in Fig. 1(c).

The physical and magnetic properties of the lowest energy configurations of the considered Co concentrations for $(ZrNd)Fe_{24-x}Co_x$ and $(ZrNd)Fe_{22-x}Ti_2Co_x$, are given in Tab. 2. In case of Co substitution in $(ZrNd)Fe_{24-x}Co_x$ a slight increase in magnetic properties is observed. For example, the total magnetic moment increases by 0.86 μ_B from Co-free to 6 Co atoms. In case of substitution in $(ZrNd)Fe_{22-x}Ti_2Co_x$, a decrease in the total magnetic moment of −0.93 μ_B is observed with the substitution of 6 Co atoms. Note that this increase (decrease) only becomes visible with the substitution of the fourth Co atom. Thus, Co at its
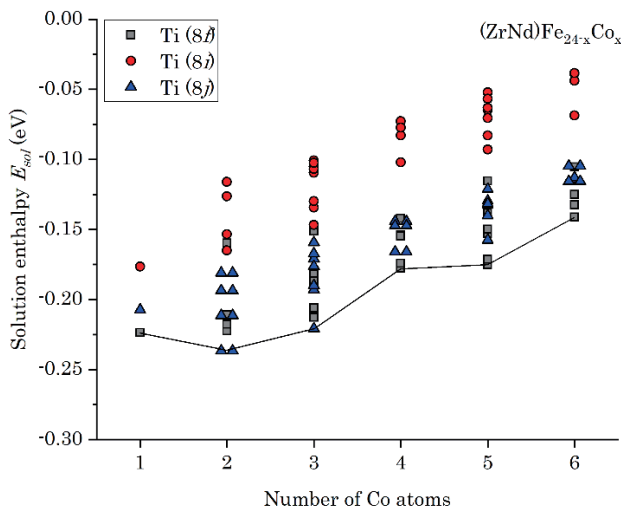

Fig. 4 Calculated Co solution enthalpies for chemical compositions with the formula $(ZrNd)Fe_{22-x}Ti_2Co_x$ according to Eq. 2.

equilibrium concentration has only a small effect on the magnetic properties. The substitution of a Ti or Co atom in $(ZrNd)Fe_{24}$ leads to a stabilization of −0.96 eV and −0.22 eV, respectively. Therefore, Co has a lower impact on the stability of the compound than Ti.

The calculated physical properties of the considered compounds are given in Tab. 3. A trend of decreasing lattice constants and cell volumes with $Nd_2Fe_{24-y}Ti_y$ > $ZrNdFe_{24-y}Ti_y$ > $Zr_2Fe_{24-y}Ti_y$ with $0 \le y \le 2$ can be seen. This trend is in good agreement with existing theoretical and experimental values.[16,20,60] This behaviour has also been previously documented by Sakuma *et al.*[11] Furthermore, an increasing volume with increasing Ti concentration is observed, which is in agreement to the calculations of Harashima *et al.*[64] The substitution of Co in the quaternary compound $ZrNdFe_{22}Ti_2$ shows a minimal increase in cell volume (by 0.03 Å³) and in the lattice constant c (by 0.015 Å), while the lattice constants a (by 0.020 Å) and b (by 0.005 Å) are slightly reduced. As mentioned above, a GGA+U treatment was also included for Nd containing compounds (see values in parenthesis in Tab. 3), which shows the same trends. In case of the bulk moduli, a softening effect of Ti can be seen. This

Fig. 3 Calculated Co solution enthalpies for chemical compositions with the formula $(ZrNd)Fe_{24-x}Co_x$ according to Eq. 2.

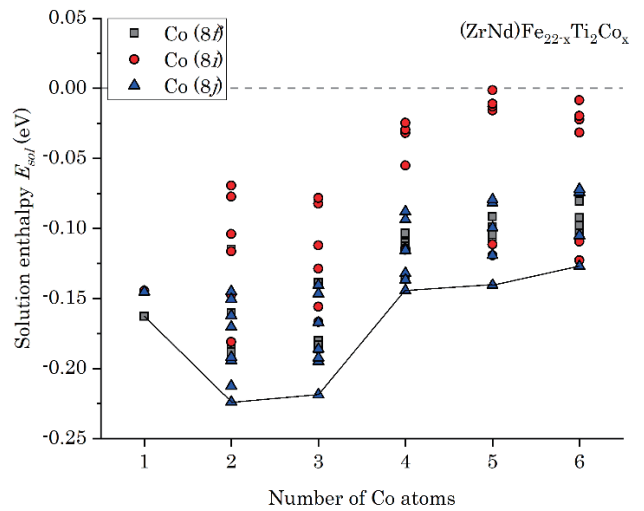**Table 3** Calculated lattice constant, cell volume and bulk modulus of the considered alloys using GGA. In case of Nd containing stable compounds GGA+U has been considered for Nd $4f$ electrons with $U = 6$ eV and is given in parenthesis.

Alloy	Lattice constants (Å)			Experimental Lattice constants (Å)		Cell volume (Å³)	Experimental Cell volume (Å³)	Bulk modulus (GPa)	Literature Bulk modulus (GPa)
	a	b	c	a	c				
Nd$_2$Fe$_{24}$ (NdFe$_{12}$)	8.535	8.535	4.671	8.574*[65]	4.907*[65]	170.13	180.37*[65]	129.45	127.96*[16]
Nd$_2$Fe$_{23}$Ti (NdFe$_{11.5}$Ti$_{0.5}$)	8.568 (8.558)	8.530 (8.533)	4.680 (4.675)	8.552*[16]	4.686*[16]	171.02 (171.06)	171.73*[16] (171.81)*[16]	128.74	127.17*[16]
Nd$_2$Fe$_{22}$Ti$_2$ (NdFe$_{11}$Ti)	8.593 (8.584)	8.535 (8.532)	4.696 (4.703)	8.574[a][66] 8.574[a][67]	4.907[a][66] 4.794[a][67]	172.19 (172.21)	176.2[a][66] 180.35[a][67]	128.89	127.20*[16]
Zr$_2$Fe$_{24}$ (ZrFe$_{12}$)	8.312	8.312	4.647			160.54		144.46	
Zr$_2$Fe$_{23}$Ti (ZrFe$_{11.5}$Ti$_{0.5}$)	8.285	8.377	4.677			162.29		139.03	
Zr$_2$Fe$_{22}$Ti$_2$ (ZrFe$_{11}$Ti)	8.258	8.433	4.708	8.358*[68]	4.715*[68]	163.93		139.58	
ZrNdFe$_{24}$ ((Zr$_{0.5}$Nd$_{0.5}$)Fe$_{12}$)	8.419	8.419	4.656			165.01		132.98	
ZrNdFe$_{23}$Ti ((Zr$_{0.5}$Nd$_{0.5}$)Fe$_{11.5}$Ti$_{0.5}$)	8.439 (8.439)	8.439 (8.440)	4.669 (4.666)			166.27 (166.20)		130.23	
ZrNdFe$_{22}$Ti$_2$ ((Zr$_{0.5}$Nd$_{0.5}$)Fe$_{11}$Ti)	8.411 (8.352)	8.497 (8.508)	4.704 (4.703)			168.08 (167.10)		130.59	
ZrNdFe$_{20}$Co$_2$Ti$_2$	8.391 (8.399)	8.492 (8.483)	4.719 (4.721)			168.11 (168.17)		133.30	
(Nd$_{0.7}$Zr$_{0.3}$)$_2$(Fe$_{0.75}$Co$_{0.25}$)$_{23}$Ti				8.536[a][20]	4.770[a][20]		173.8[a][20]		

*Theoretical references are represented by *.
[a] X-ray diffraction (XRD) analysis at 300 K.

effect occurs again not only in the Nd$_2$Fe$_{24-y}$Ti$_y$ compounds but also in the Zr$_2$Fe$_{24-y}$Ti$_y$ compounds as well as in the compounds containing both Nd and Zr with ZrNdFe$_{24-y}$Ti$_y$ (y: $0 \leq y \leq 2$) (see Tab. 3).

3.2 Total magnetic moment and magnetization

The magnetization of the chosen compounds is calculated distinguishing between the total magnetic moment and the saturation magnetization. The total magnetic moment, expressed in Bohr magnetons (μ_B) per formula unit, is the cumulative sum of the magnetic moments of the individual atoms. The saturation magnetization, measured in Tesla (T), can be derived from the density of the compound (ρ), the Avogadro constant (N_A), the molecular weight (M) and the average magnetic moment per atom m^{tot}_{atom} the compound:

$$\mu_0 M_S = m^{tot}_{atom} \mu \frac{\rho \cdot N_A}{M_{alloy}}. \tag{3}$$

The calculated intrinsic magnetic properties, including the total magnetic moment (m_{tot}), the spin magnetic moment of the atoms in $2a$ position (m^{2a}_{spin}) and the saturation magnetization ($\mu_0 M_S$), are given in Tab. 4. These values are compared with previous theoretical and experimental data for analogous compounds. It is noteworthy that the PBE functional tends to overestimate the magnetic moments[69], placing the calculated values within the expected range. This overestimation can be assessed in case of NdFe$_{11}$Ti by comparison with literature values. Contrarily, for Zr$_2$Fe$_{24-y}$Ti$_y$ (y: $0 \leq y \leq 2$) compounds such an assessment is not possible, since neither theoretical nor experimental values have been published so far. It should also be noted that even the relaxed structure does not guarantee that the magnetic properties are correctly reproduced.

In case of quaternary ZrNdFe$_{24-y}$Ti$_y$ (y: $0 \leq y \leq 2$) alloys, it is possible to estimate m_{tot} as both experimental and

theoretical values are available for similar compounds and fall within the expected range (see Tab. 4). In contrast, for Zr$_2$Fe$_{24-y}$Ti$_y$ compounds, the magnetic moments of Fe and Ti are close to those of Nd$_2$Fe$_{24-y}$Ti$_y$ (y: $0 \leq y \leq 2$) compounds, considering the structural difference only at the $2a$ sites with Zr at -0.47 μ_B and Nd at -0.27 μ_B.

The GGA calculations, using an in-core treatment for f electrons, give reasonable m_{tot} for NdFe$_{11-y}$Ti$_y$ compounds. In particular, the calculated m_{tot} for NdFe$_{11}$Ti is 24.84 μ_B, while the experimentally measured m_{tot} by Skokov et al.[33] is 23.43 μ_B. However, the in-core approximation neglects the contribution of the f electrons. By including f electrons and using the GGA+U treatment, where they are considered to be fully localized, a revised m_{tot} of 25.04 μ_B (including the orbital magnetic moment) is calculated. In addition, the GGA+U treatment yields a saturation magnetization of 1.69 T, in agreement with experimentally determined M_S of 1.38 T to 1.70 T.[33,60,66,67]

In the context of the GGA+U approximation, a reduced spin magnetic moment is observed with a magnitude of the Nd ion of -3.30 μ_B. This reduction, approximately -3.0 μ_B from the GGA value of -0.27 μ_B, is attributed to the influence of the f electrons. Nevertheless, the results for both treatments are acceptable compared to experimental values. It is important to note that the calculated results are based on the summation of the orbital magnetic moment of the Nd-$4f$ electrons with $g_j \cdot J = |L - S| = 3.273$ μ_B.

The substitution of Zr atoms into the 1:12 phase results in an average reduction of the total magnetic moment from 2.25 μ_B/f.u. (ZrNdFe$_{24-y}$Ti$_y$) to 4.21 μ_B/f.u. (Zr$_2$Fe$_{24-y}$Ti$_y$). In GGA this reduction can be attributed to the comparatively lower magnetic moment of Zr (-0.47 μ_B) compared to Nd (-0.27 μ_B). Nevertheless, in the GGA+U treatment, the inclusion of f electrons leads to a reduction in the magnetic moment of Nd to -3.3 μ_B, showing an opposite trend.

Table 4 Calculated spin magnetic moments at rare-earth site m^{2a}_{spin}, total magnetic moments m_{tot} (μB/f.u.), maximum energy product $|BH|_{max}$ (kJ/m^3) and saturation magnetization $\mu_0 M_S$ (T) with comparison against available experimental data. In case of Nd containing compounds GGA+U with U = 6 eV is applied to Nd 4f electrons only and results are given in parenthesis.

Alloy	m^{2a}_{spin} (μB/f.u.)	m_{tot} (μB/f.u.)	Experimental m_{tot} (μB/f.u.)	$\mu_0 M_S$ (T)	Experimental $\mu_0 M_S$ (T)	$\|BH\|_{max}$ (kJ/m^3)	Experimental $\|BH\|_{max}$ (kJ/m^3)
Nd$_2$Fe$_{24}$ (NdFe$_{12}$)	-0.27	29.67	27.2*[70], 29.15*[46], 31.20*[65]	2.03	1.73*[70], 1.99*[46], 2.01*[65]	821.55	818*[16]
Nd$_2$Fe$_{23}$Ti (NdFe$_{11.5}$Ti$_{0.5}$)	-0.27 (-3.29)	27.14 (27.31)		1.85 (1.86)		680.30 (688.49)	683*[16], 701*[16]
Nd$_2$Fe$_{22}$Ti$_2$ (NdFe$_{11}$Ti)	-0.28 (-3.30)	24.84 (25.04)	21.27[a][66], 21.90[b][67], 23.43[c][33], 24.10*[71], 24.50*[46], 25.24[d][60], 26.30*[65]	1.68 (1.69)	1.38[a][66], 1.48[b][67], 1.58[c][33], 1.63*[71], 1.65*[46], 1.70[d][60], 1.70*[65]	562.30 (571.39)	438*[46], 569*[16], 575*[16]
Zr$_2$Fe$_{24}$ (ZrFe$_{12}$)	-0.47	24.98		1.81		654.10	
Zr$_2$Fe$_{23}$Ti (ZrFe$_{11.5}$Ti$_{0.5}$)	-0.46	23.13		1.66		548.87	
Zr$_2$Fe$_{22}$Ti$_2$ (ZrFe$_{11}$Ti)	-0.45	21.28		1.51		455.19	
ZrNdFe$_{24}$	-0.50 (m^{2a}_{Zr}), -0.26 (m^{2a}_{Nd})	27.16		1.92	1.93* (Zr$_{0.1}$)[68], 1.91* (Zr$_{0.2}$)[68], 1.89* (Zr$_{0.3}$)[68]	732.20	741* (Zr$_{0.1}$)[68], 726* (Zr$_{0.2}$)[68], 711* (Zr$_{0.3}$)[68]
ZrNdFe$_{23}$Ti	-0.50 (m^{2a}_{Zr}), -0.26 (m^{2a}_{Nd}) ((-0.50 (m^{2a}_{Zr})), (-3.27 (m^{2a}_{Nd})))	24.77 (24.82)		1.74 (1.74)		599.63 (602.83)	
ZrNdFe$_{22}$Ti$_2$	-0.49 (m^{2a}_{Zr}), -0.27 (m^{2a}_{Nd}) ((-0.48 (m^{2a}_{Zr})), (-3.31 (m^{2a}_{Nd})))	23.10 (23.28)		1.60 (1.62)		510.17 (524.51)	
ZrNdFe$_{20}$Co$_2$Ti$_2$	-0.49 (m^{2a}_{Zr}), -0.26 (m^{2a}_{Nd}) ((-0.49 (m^{2a}_{Zr})), (-3.28 (m^{2a}_{Nd})))	23.22 (23.28)		1.61 (1.61)		515.62 (517.70)	
Nd$_2$(Fe$_{0.75}$Co$_{0.25}$)$_{23}$Ti			25.41[d][63]		1.63[d][63]		529[d][63]
(Nd$_{0.7}$Zr$_{0.3}$)$_2$(Fe$_{0.75}$Co$_{0.25}$)$_{23}$Ti			24.43[d][63]		1.63[d][63], 1.66[d][20]		529[d][63], 548[d][20]

Theoretical references are represented by.
[a] Extraction sample magnetometer analysis at 1.5 K.
[b] Mössbauer measurement at 4.2 K.
[c] Single crystal, physical property measurement system (PPMS) measured at 10 K.
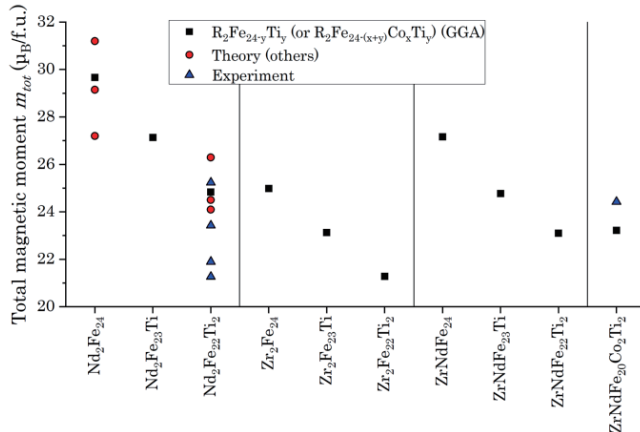[d] Vibrating sample magnetometer (VSM) analysis at 4.2 K.

Fig. 5 Total magnetic moments of R$_2$Fe$_{24-y}$Ti$_y$ (R: Zr and Nd; y: $0 \leq y \leq 2$). Since GGA+U calculations do not change the results significantly, only GGA results are given. The red circles show theoretical data[46,65,70,71] for the alloys from others and the blue triangles show experimental data[11,33,60,66,67] for the alloys. Here all literature values correspond to the same compounds. Only the experimental m_{tot} at ZrNdFe$_{20}$Co$_2$Ti$_2$ corresponds to the (Zr$_{0.3}$Nd$_{0.7}$)$_2$(Fe$_{0.75}$Co$_{0.25}$)$_{23}$Ti compound.

The effect of the Ti substitution on the total magnetic moments of the compounds studied is shown in Fig. 5. In both GGA and GGA+U calculations, the total magnetization of Ti atoms is approximately −1.1 μB. This phenomenon is due to the antiferromagnetic orientation of Ti atoms with respect to the Fe atoms. In particular, there is an observable trend that the total magnetic moment decreases with increasing concentration of Ti in compounds. The trend calculated in the m_{tot} values of the Nd$_2$Fe$_{24-y}$Ti$_y$ (y: $0 \leq y \leq 2$) compounds aligns with the findings of our previous research.[16] For all considered compounds, there is a consistent decrease in the total magnetic moment, averaging 2-3 μB/f.u. per Ti atom.

The effect of Co on the total magnetic moment is relatively modest, as shown in Tabs. 2 and 4. A comparison between the m_{tot} of ZrNdFe$_{22}$Ti$_2$ and ZrNdFe$_{20}$Co$_2$Ti$_2$ shows only an increase of 0.12 μB/f.u. in GGA. This finding is similar for the GGA+U approach as well. The effect of Co on the magnetic properties depends on the presence of Ti in the compound. When combined with Ti, a decrease in the magnetic properties can be seen, while in the absence of Ti, an increase is calculated.

3.3 Maximum energy product $|BH|_{max}$

A magnet consists of magnetic domains, which are small regions in which the magnetic moment is oriented in only one direction. The arrangement of these domains
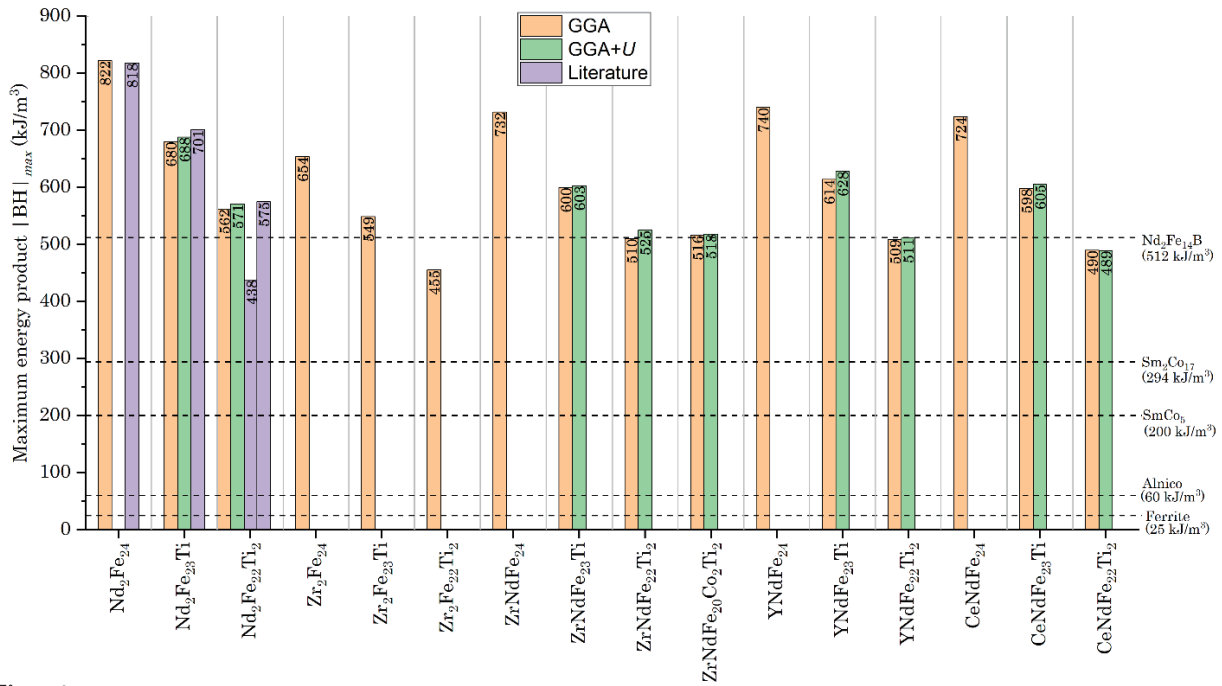
Fig. 6 Theoretical maximum energy product $|BH|_{max}$ values for the considered compounds and the literature for comparison[16,46]. In addition to conventional GGA, GGA+U with $U = 6$ eV has been considered for stable Nd containing alloys. Experimental values[75,77] of the most common hard magnets are given as horizontal dashed lines.

is called the microstructure, which is the origin of the extrinsic magnetic properties.[72,73] The maximum energy product $|BH|_{max}$ is one of the key performance measures for permanent magnets. It is an important figure-of-merit for the strength of permanent magnetic materials and a magnet should be designed to operate near the $|BH|_{max}$ point in order to maximize its efficiency. In addition, $|BH|_{max}$ serves as a reflective indicator of the upper limit of magnetic energy that can be stored in free space by a unit volume of permanent magnet.[74] It is furthermore the optimal product of the two extrinsic properties remanence B_r and coercivity H_c and can be estimated from the hysteresis loop. In the case of an ideal quadratic hysteresis loop, there is a relationship between $|BH|_{max}$ and M_S, since in that case the remanence magnetization M_r is maximum and equals M_S ($\mu_0 M_r = \mu_0 M_S$). Thus, $|BH|_{max}$ can theoretically be calculated as follows:[72,75]

$$|BH|_{max} = \frac{\mu_0 M_S^2}{4}, \qquad (4)$$

where μ_0 is the vacuum permeability ($\mu_0 = 4\pi \cdot 10^{-7}$ NA^{-2}). The calculated $|BH|_{max}$ values of the selected compounds are shown in Tab. 4 and Fig. 6.

Figure 6 shows the $|BH|_{max}$ values of known hard magnets as a reference. A hard magnetic compound can be considered as promising once its maximum energy product exceeds 400 kJ/m³. Elevated $|BH|_{max}$ values are calculated in Ti-free RFe₁₂ compounds where R represents Y, Zr and Ce. The substitution of a single Ti atom by Fe (representing 3.8 at. % in the 2 f.u. supercell) results in an average reduction in $|BH|_{max}$ of about 120 kJ/m³. The substitution of the second Ti atom (representing 7.7 at. % in the 2 f.u. supercell) further

reduces the $|BH|_{max}$ by a 100 kJ/m³.

The lack of experimental $|BH|_{max}$ data precludes direct comparison with theoretical values. However, there are alternative theoretical and experimental results for analogous compounds that facilitate comparative assessments. Körner *et al.*[46] used the tight-binding linear-muffin-tin-orbital atomic-sphere approximation (TB-LMTO-ASA) to calculate $|BH|_{max}$ for various 1:12 phases. Their calculations for NdFe₁₁Ti yields a $|BH|_{max}$ of 438 kJ/m³, where our GGA (GGA+U) calculation finds 562 kJ/m³ (575 kJ/m³). Our current $|BH|_{max}$ calculation is in good agreement with the research of Herper *et al.*[76], who calculated 490 kJ/m³.

In case of Zr₂Fe₂₄₋ᵧTiᵧ (y: 0 ≤ y ≤ 2) compounds, the calculated $|BH|_{max}$ values are ≥ 450 kJ/m³. However, these ternary $|BH|_{max}$ values are about 130 kJ/m³ lower than the ternary Nd₂Fe₂₄₋ᵧTiᵧ (y: 0 ≤ y ≤ 2) compounds. As an example, the ratio of ZrFe₁₁Ti to NdFe₁₁Ti is given as 455 kJ/m³ and 562 kJ/m³, respectively. As expected, the quaternary ZrNdFe₂₄₋ᵧTiᵧ compounds fall within the range defined by the $|BH|_{max}$ values of the R₂Fe₂₄₋ᵧTiᵧ compounds (where R: Nd and Zr, y: 0 ≤ y ≤ 2), making them promising candidates. A comparison between the calculated $|BH|_{max}$ of ZrNdFe₂₃Ti (600 kJ/m³) and the experimentally determined value of (Zr₀.₃Nd₀.₇)₂(Fe₀.₇₅Co₀.₂₅)₂₃Ti (548 kJ/m³)[20] shows a remarkable agreement.

In case of Co substitution, the effect is challenging to determine due to the limited literature available. When comparing the calculated $|BH|_{max}$ of ZrNdFe₂₂Ti₂ and ZrNdFe₂₀Co₂Ti₂, there is a minimal difference. Depending on the method used, there is a slight increase for GGA or decrease for GGA+U in the maximum energy product of about 6 kJ/m³. For a comparison with literature, the compound (Nd₀.₇Zr₀.₃)₂(Fe₀.₇₅Co₀.₂₅)₂₃Ti is
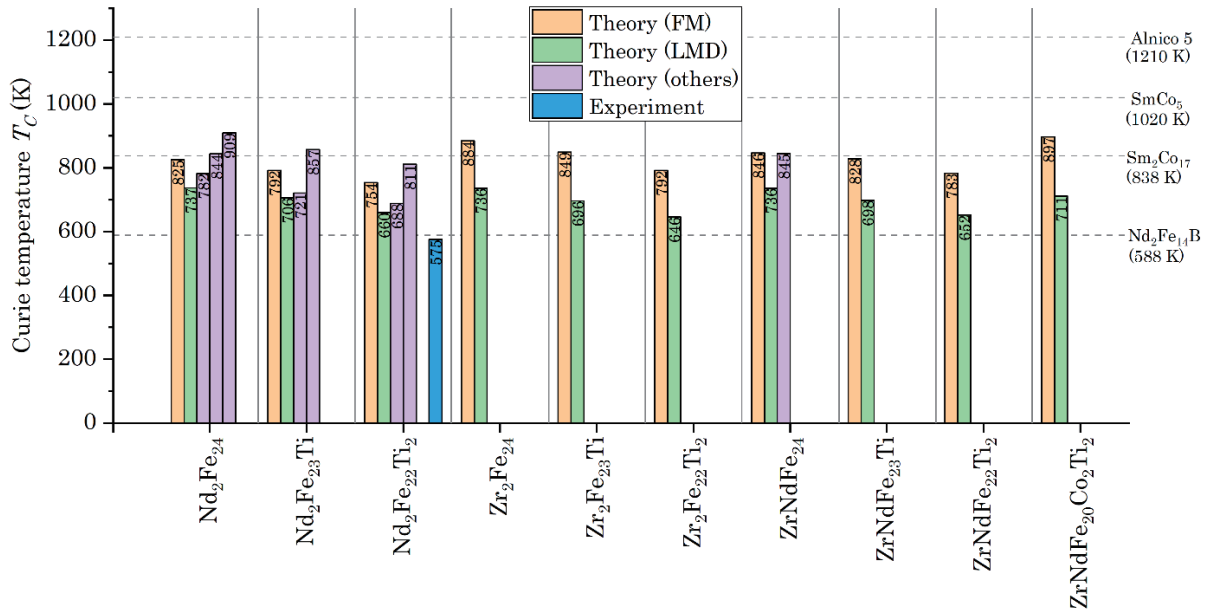
Fig. 7 Calculated Curie temperatures T_C for all considered 1:12 phases. The exchange interaction energies have been calculated for both ordered ferromagnetic (FM) and disordered local momentum (LMD) states, and the lattice information comes from the theoretically relaxed calculations (see Tab. 3). The literature data is taken from[16,66,68]. Here, all literature values refer to the same compounds. Only the theoretical T_C for ZrNdFe24 corresponds to the $(Zr_{0.3}Nd_{0.7})_2Fe_{24}$ compound.

considered. However, as this compound contains less Zr and Ti and more Co, the previous effects of the elements must be taken into account. Due to the effects of Zr and Ti, a higher $|BH|_{max}$ can be assumed for the literature compound. The $|BH|_{max}$ of the literature compound of 529 [63] and 548 kJ/m³ [20] are higher than the calculated $|BH|_{max}$ of the compounds $ZrNdFe_{22}Ti_2$ and $ZrNdFe_{20}Co_2Ti_2$, but lower than that of $ZrNdFe_{23}Ti$. Based on this ordering of the literature $|BH|_{max}$, a reduction due to Co can be assumed. This reduction in combination with Ti can also be seen in Tab. 2.

In Fig. 6, the $|BH|_{max}$ values of well-known hard magnets are provided as a reference. A comparison between the well-known hard magnet $Nd_2Fe_{14}B$, with a $|BH|_{max}$ of 688 kJ/m³ [31], and the quaternary alloy $ZrNdFe_{11}Ti$ shows that the calculated $|BH|_{max}$ are smaller than the theoretical value of $Nd_2Fe_{14}B$. Furthermore, the quaternary Zr compound can be compared with the Y and Ce quaternaries calculated in our previous work.[16] It is observed that in the case of $(R,Nd)Fe_{11.5}Ti_{0.5}$ (R: Y, Zr and Ce) alloys, the Y-containing alloy exhibits the highest $|BH|_{max}$ at 628 kJ/m³, followed by the Ce and Zr-containing alloys. For the $(R,Nd)Fe_{11}Ti$ (R: Y, Zr and Ce) alloys, a trend emerges where the Zr-containing alloy has the highest $|BH|_{max}$ at 510 kJ/m³, followed by the Y and Ce alloys.

3.4 Curie temperature

In addition to a strong magnetization, a high Curie temperature T_C is another desired intrinsic magnetic property. The well-known and widely used $Nd_2Fe_{14}B$ magnet has a relatively low experimental T_C of 588 K[75], while traditional RE-based permanent magnets have higher T_C (e.g. $SmCo_5$ with 1020 K[75]). Finding an Nd-lean RE magnet with a better balance between saturation magnetization and Curie temperature thus

deserves extensive efforts.

To calculate T_C, an effective spin Heisenberg model is chosen, which is solved in the mean field approximation (MFA). In this Heisenberg model the Hamiltonian of the spin-spin interaction is given by $H = -\sum_{i \neq j} J_{ij} \vec{S_i} \vec{S_j}$, where $\vec{S_i}$ and $\vec{S_j}$ correspond to the spin of place i and j, respectively. J_{ij} corresponds to the exchange coupling constant between the two sites i and j and was calculated with AkaiKKR.[38] The absolute value of the magnetic ordering temperature T_C resulting from MFA is $k_B T_C = \frac{3}{2} \cdot J_0$, where k_B is the Boltzmann constant. J_0 is the sum of J_{ij} and is therefore the total effective exchange of a given lattice site connected to all others.

One of the main drawbacks of the evaluation of J_{ij} when considered the FM configuration, is the systematic overestimation of T_C (approx. 45%). Therefore, as an alternative to the FM states, the local moment disorder (LMD) approach is considered as well. In the framework of the KKR-CPA method, the concept of LMD state (also called disorder local moment (DLM[78])) is conveniently used to describe the paramagnetic state of a ferromagnet above T_C.[79] Nevertheless, magnetic moments survive and do not vanish. As an advantage of the KKR based on Green's function theory, the exchange interaction energies for such situations and the Curie temperature for both FM and LMD states can be calculated.

The calculated Curie temperatures are shown in Fig. 7, with the relevant theoretical and experimental data reported in the literature. The horizontal dashed lines represent the T_C of established permanent magnets for comparative analysis. As shown, the calculated FM ground state approximation in this work overestimates for most of the cases as expected. However, calculating the T_C by considering the LMD as the ground state, the agreement improves significantly. This overestimation is due to the challenges of describing the delocalized

electronic state in the magnetism of intermetallics[80,81] based on localized degrees of freedom. In addition, the exchange coupling between local moments is calculated for the ground state and this assumption does not need to be valid for high temperatures near T_C.

Miyake *et al.*[82] highlighted the accuracy of LMD calculations is intricately linked to the crystal structure of the 1:12 phase, claiming that in certain cases LMD values exhibit greater precision than their FM counterparts. This correlation appears to be due to variations in spin fluctuation near magnetic transitions, although a full understanding of this phenomenon is currently lacking and warrants further investigation. For the further details about the relationship between LMD performance and both crystal structure and transition metals we refer Ref.[82]. In case of $Zr_2Fe_{24-y}Ti_y$ (y: $0 \leq y \leq 2$) compounds, the lack of available literature data necessitates that calculated values be considered as indicative measures of T_C only. In the specific case of $(Zr_{0.3}Nd_{0.7})_2(Fe_{0.75}Co_{0.25})_{23}Ti$, Suzuki *et al.*[63] approximate a T_C of >840 K, implying that the FM values for $ZrNdFe_{24-y}Ti_y$ (y: $0 \leq y \leq 2$) and $ZrNdFe_{20}Co_2Ti_2$ compounds are more likely than the LMD results.

Similar to the trends calculated for m_{tot} and $|BH|_{max}$, the Curie temperature shows a decrease with increasing Ti concentration, as shown in Fig. 7. The Curie temperature decreases approximately 45 K per Ti atom (3.8 at. %), which is consistent with the average decrease found in our previous research[16]. The theoretical FM (LMD) results show the following trend, with calculated T_C values of 792 (646), 783 (652) and 754 (660) K for $R_2Fe_{22}Ti_2$ (R₂: Zr_2, $ZrNd$, Nd_2, respectively). In the absence of comprehensive literature data, the trend of the calculated compounds is estimated from analogous compounds such as $(Zr_{0.3}Nd_{0.7})_2(Fe_{0.75}Co_{0.25})_{23}Ti$[63] and $Nd_2Fe_{24-y}Ti_y$ (y: $0 \leq y \leq 2$).[16,82]

The substitution of 3.8 at. % Nd with Zr results in the average reduction in the T_C as 6 K for LMD and the average increase as 29 K for FM. The complete substitution of Nd by Zr (7.7 at. %) increases the average reduction in the T_C to 8 K for LMD and the average increase to 51 K for FM. Due to a lack of data, these trends cannot be directly compared with the literature. Nevertheless, Schönhöbel *et al.*[83] experimentally investigated the effects of substitution of Nd and Zr into $SmFe_{11}V$. This study showed a decrease in T_C for 3.1 at. % substitution of Sm as 32 K for Nd and as 26 K for Zr. Subsequently, Nd lowers T_C more than Zr. Therefore, a slight increase in T_C is expected when Nd is substituted for Zr. When evaluating the Curie temperatures, the quaternary compound $ZrNdFe_{22}Ti_2$ with 652 K (LMD) and 783 K (FM) exceeds the experimental T_C (588 K) of $Nd_2Fe_{14}B$, but not the theoretical T_C of 1050 K.[84]

A Co substitution of 7.7 at. % in $ZrNdFe_{22}Ti_2$ to $ZrNdFe_{20}Co_2Ti_2$ causes an increase in the Curie temperature of about 85 K (see Fig. 7). This increase is also observed by Gjoka *et al.*[85], who measured an increase of about 50 K per 7.7 at. % Co in $Nd_{0.4}Zr_{0.6}Fe_{10-x}Co_xSi_2$.

In summary, due to the expected overestimation by considering the FM states, all considered compounds have T_C values slightly below to above the critical experimental temperature of $Nd_2Fe_{14}B$ (588 K).[75]

Additionally, the theoretical T_C of above 950 K[86] for Sm_2Co_{17} can potentially be approached through Co substitution.

3.5 Magnetocrystalline Anisotropy Energy

The next magnetic property considered in this section is the magnetocrystalline anisotropy energy (MAE). The MAE can be determined from the magnetic force theorem[87] or by calculating the energy difference of the magnetization directions. In this study the latter approach is used to calculate the MAE. Equation (5) is used to calculate the energy difference from the axis with the easiest magnetization ([001]) to the axis of the hardest magnetization ([010]). Furthermore, in addition to being defined as in Eq. (5), which follows the general definition, the MAE is determined between the easiest direction to magnetize ([001]) and the easiest direction within the plane perpendicular to the easiest direction ([100]). This definition ensures that MAE values are consistent with uniaxial anisotropy and resulting MAE values are given in parenthesis. Using GGA+U for $Nd_2Fe_{22}Ti_2$ results in energy differences of $7.2 \cdot 10^{-4}$ eV for [010] to [001] and $3.7 \cdot 10^{-4}$ eV for [100] to [001]. This means that the highest energy difference is by a change from [010] and [001]. The equations used to calculate the MAE is as follows:

$$\Delta E_{MAE} = E_{[010]} - E_{[001]}, \tag{5}$$

where $E_{[001]}$ and $E_{[010]}$ are the total energies of the magnetization directions [001] and [010] of the supercell, respectively.

From the total energies and the resulting energy differences the anisotropy constant K_1 and the anisotropy field H_a can be calculated. The anisotropy energy can be written as:

$$\Delta E_{MAE} = K_1 \cdot sin(\phi)^2, \tag{6}$$

where ϕ is the angle between the direction of magnetization and the easiest axis to magnetize. In this formulation, only the dominant term containing K_1 is presented, providing a level of accuracy deemed appropriate for this particular scenario. All phases considered within the 1:12 configuration exhibit uniaxial anisotropy, as indicated by K_1 being greater than zero. The higher order anisotropy constants are considered negligible due to the significant difference in magnitude between K_1 and K_2, with K_2 being almost two orders of magnitude smaller than K_1. Consequently, the characterization of magnetocrystalline anisotropy (MCA) can be effectively captured by the singular parameter K_1 (for more details see[88]). A positive (or negative) value of K_1 indicates uniaxial (or planar) anisotropy.

The anisotropy field H_a corresponds to the upper limit of the coercivity and can be calculated as follows:

$$H_a = \frac{2K_1}{\mu_0 M_S}. \tag{7}$$

Table 5 Calculated theoretical magnetocrystalline anisotropy constant K_1 according to Eq. 6, anisotropy field H_a according to Eq. 7 and magnetic hardness factor κ from Eq. 8 for stable compounds with available experimental data. The values are given for both GGA and LSDA treatments for the exchange–correlation potential and GGA+U (U = 6 eV) results are reported in parenthesis for Nd contained compounds. The experimental value of K_1 and κ of well known hard magnets are also given for comparison.

Alloy	K_1 GGA (MJ/m³)	K_1 LSDA (MJ/m³)	Experimental K_1 (MJ/m³)	H_a GGA (T)	H_a LSDA (T)	Experimental H_a (T)	κ GGA	κ LSDA	Experimental κ
Nd$_2$Fe$_{22}$Ti$_2$	0.34[100]	1.42[100]	0.61* [16]	0.41[100]	1.68[100]	0.72* [16]	0.35[100]	0.71[100]	0.52* [16]
(NdFe$_{11}$Ti)	0.67[010]	1.68[010]	1.41** [16]	0.80[010]	2.00[010]	1.86** [16]	0.49[010]	0.77[010]	0.88** [16]
			1.78^{b} [33]			1.9^{a} [90]			
						2.0^{a} [90]			
Zr$_2$Fe$_{22}$Ti$_2$	1.10[100]	1.61[100]		1.45[100]	2.13[100]		0.69[100]	0.84[100]	
(ZrFe$_{11}$Ti)	2.44[010]	2.47[010]		3.22[010]	3.27[010]		1.03[010]	1.04[010]	
ZrNdFe$_{22}$Ti$_2$	0.55[100]	1.56[100]		0.69[100]	1.95[100]		0.46[100]	0.78[100]	
((Zr,Nd)Fe$_{11}$Ti)	2.16[010]	2.41[010]		2.69[010]	3.01[010]		0.92[010]	0.97[010]	
ZrNdFe$_{20}$Co$_2$Ti$_2$	1.08[100]	1.43[100]		1.34[100]	1.78[100]		0.65[100]	0.74[100]	
((Zr,Nd)Fe$_{10}$CoTi)	1.97[010]	2.08[010]		2.44[010]	2.58[010]		0.87[010]	0.90[010]	
(Zr$_{0.3}$Nd$_{0.7}$)$_2$(Fe$_{0.75}$Co$_{0.25}$)$_{23}$Ti			1.41^{c} [20]			1.7^{c,d} [20]			0.71^{c} [20]
Nd$_2$Fe$_{14}$B			4.9^{e} [89]						1.54^{e} [89]
Sm$_2$Co$_{17}$			4.2^{e} [89]						1.89^{e} [89]
SmCo$_5$			17.0^{e} [89]						4.40^{e} [89]
Alnico 5			0.32^{e} [89]						0.45^{e} [89]

[010]Calculated using directions [001] vs [010].
[100]Calculated using directions [001] vs [100].
*Theoretical GGA+U references.
**Theoretical LSDA references.
^{a}Derived from magnetization curve at 300 K.
^{b}Single Crystal, Physical Property Measurement System (PPMS) measured at 10 K.
^{c}Calculated from source data.
^{d}Calculated out of experimental $\mu_0 M_S$ using the law of approaching saturation.
^{e}Properties measured at 300 K.

H_a reflects an important property of a permanent magnet and should be as high as possible. It is important to note that the values calculated here for K_1 and M_S are valid for T= 0 K. This excludes the temperature dependence of H_a.

With the anisotropy constant K_1 and the saturation magnetization M_S, the magnetic hardness factor κ can be calculated. This is done using the following equation:[89]

$$\kappa = \sqrt{\frac{K_1}{\mu_0 M_S^2}}. \tag{8}$$

The resulting κ can be used to estimate a materials potential as a permanent magnet. A magnetic compound can be classified as a soft ($\kappa < 0.1$), semi-hard ($0.1 < \kappa < 1$), or hard ($\kappa > 1$) magnet. Materials with $\kappa > 1$ are suitable for use as permanent magnets, regardless of their shape. On the other hand, those in the semi-hard range ($0.1 < \kappa < 1$) have shape and dimensional limitations, such as Alnico magnets.[87]

Previously we found that MAE increases with increasing Ti concentration.[16] Therefore, we use this finding here and only consider compounds with high Ti concentration (7.7 at. %), as these are also the most likely stable compounds. Table 5 shows the calculated anisotropy constant (K_1), anisotropy field (H_a) and hardness factor (κ) obtained by GGA+U and LSDA.

For the NdFe$_{11}$Ti compound, the GGA+U calculation yielded an anisotropy constant of 0.67 (0.34 for [100] vs [001]) MJ/m³, which significantly underestimated the experimentally measured K_1 of 1.78 MJ/m³ by Skokov *et al*.[33]. Therefore, we considered LSDA to further investigate the MAE. The LSDA calculation results a significant increase in K_1 to 1.68 (1.42 for [100] vs

[001]) MJ/m³, which is in better agreement with the literature.

The substitution of Nd with Zr increases the MAE compared to NdFe$_{11}$Ti. The quaternary (Zr,Nd)Fe$_{11}$Ti has a K_1 potentially exceeding the experimental value of 1.78 MJ/m³ for NdFe$_{11}$Ti, with a difference of 0.38 MJ/m³ for GGA+U and 0.63 MJ/m³ for LSDA. In case of the Zr-based 1:12 compound, ZrFe$_{11}$Ti, K_1 increases by a further 0.28 MJ/m³ for GGA+U and by 0.06 MJ/m³ for LSDA. However, in case of [100] vs [001], the calculated K_1 of the Zr-containing compounds do not reach to the experimental K_1 of NdFe$_{11}$Ti. The values calculated for (Zr,Nd)Fe$_{11}$Ti and ZrFe$_{11}$Ti in the case of GGA+U are 1.23 and 0.68 MJ/m³ lower, respectively. The LSDA K_1 are also smaller by 0.22 and 0.17 MJ/m³ than the 1.78 MJ/m³ of NdFe$_{11}$Ti. The evaluation of the Zr-containing phase is challenging due to a lack of available literature. The small difference between the LSDA value of (Zr,Nd)Fe$_{11}$Ti (2.41 MJ/m³) and the K_1 of ZrFe$_{11}$Ti (2.44 GGA+U and 2.47 MJ/m³ LSDA) suggests that the accuracy of the GGA+U method increases with higher Zr content. This is also supported by the fact that the difference between the GGA+U and LSDA values for K_1 decreases as the Zr content increases, from 1.01 (1.08 for [100] vs [001]) MJ/m³ for Nd$_2$Fe$_{22}$Ti$_2$ to 0.25 (1.01 for [100] vs [001]) MJ/m³ for ZrNdFe$_{22}$Ti$_2$ and 0.03 (0.51 for [100] vs [001]) MJ/m³ for Zr$_2$Fe$_{22}$Ti$_2$.

The impact of Co on the K_1 can be examined by the difference between (Zr,Nd)Fe$_{11}$Ti and (Zr,Nd)Fe$_{10}$CoTi compounds. In the case of GGA (LSDA) treatment K_1 reduces 0.19 (0.33) MJ/m³. Note that this reduction is raised by a low Co concentration, *i.e.* 7.7 at. %. Suzuki *et al*.[63] observed a slight decrease in H_a of about 0.06 MJ/m³ due to the substitution of 2.3 at. % Co in Nd(Fe$_{1-y}$Co$_y$)$_{11}$Ti. Since H_a and K_1 are directly proportional (see Eq. 7), a decrease in K_1 can be expected. Using the data presented

in the study by Suzuki *et al.*[63], a reduction of about 0.3 MJ/m^3 can be derived for K_I, which shows a good agreement with the calculated LSDA value following Eq. (5). In case of following the anisotropy from the easiest perpendicular to the easiest in plane direction, this effect is also visible to a lesser extent, with a reduction in case of LSDA of 0.13 MJ/m^3.

In addition, K_I values between RFe$_{11}$Ti alloys (R: Y, Zr, Ce and Nd) shows a clear trend in GGA+U values: Nd (0.67 MJ/m^3) < Y (0.92 MJ/m^3 [16]) < Ce (2.08 MJ/m^3 [16]) < Zr (2.16 MJ/m^3). Corresponding LSDA values show a parallel trend: Nd (1.68 MJ/m^3) < Y (1.73 MJ/m^3 [16]) < Ce (2.12 MJ/m^3 [16]) < Zr (2.41 MJ/m^3). In particular, Zr induces the most significant increase in K_I. The K_I obtained for Zr-containing compounds is considered to be reasonably, especially when compared to the Ce compound. However, when uniaxial anisotropy is ensured, the trends change as Zr then shows smaller values than Ce by 0.51 MJ/m^3 and Y by 0.12 MJ/m^3 in the case of LSDA and a smaller value than Ce by 0.98 MJ/m^3 in case of GGA+U.

In the context of this study, which includes quaternary compounds and draws comparisons with previous research[16], the trend calculated in the GGA+U (and LSDA) treatments is as follows: (Y,Nd)Fe$_{11}$Ti with 0.91 (1.65)[16] < (Ce,Nd)Fe$_{11}$Ti with 1.35 (1.61)[16] < (Zr,Nd)Fe$_{11}$Ti with 2.16 (2.41) MJ/m^3. The position of (Zr,Nd)Fe$_{11}$Ti in this trend is reversed when the values of calculations [100] to [001] are considered.

In Eq. 7 the anisotropy field (H_a) is determined by the anisotropy constant (K_I) and the saturation magnetization (M_S). It is noteworthy that, as with K_I, there is a shortage of literature for the comparison of Zr-containing compounds. In case of NdFe$_{11}$Ti, comparisons can be made with the experimental H_a values obtained by Bouzidi *et al.*[90] (1.9 T) and Akayama *et al.*[60] (2.0 T). The calculated H_a from the GGA+U treatment (0.80 (0.41 for [100] vs [001]) T) is significantly lower than the literature value, while the LSDA treatment gives a H_a of 2.00 (1.68 for [100] vs [001]) T, showing good agreement. For ZrFe$_{11}$Ti, (Zr,Nd)Fe$_{11}$Ti and (Zr,Nd)Fe$_{10}$CoTi, the GGA+U (and LSDA) treatments following the easiest perpendicular [001] and the hardest directions [010] give H_a values of 3.22 (3.27), 2.69 (3.01) and 2.44 (2.58) T, respectively. Using the easiest perpendicular [001] and the easiest in-plane direction [100], the H_a values are 1.10 (1.61), 0.55 (1.56) and 1.08 (1.43) T, respectively. These H_a values show similar trends to those calculated for K_I. Analogous trends are evident when comparing the Y and Ce compounds from our previous research[16]. For the quaternary compounds the H_a increases with GGA+U (LSDA) treatment as follows: (Zr,Nd)Fe$_{11}$Ti with 0.55 (1.56) ([100] to [001]) < (Y,Nd)Fe$_{11}$Ti with 1.13 (2.33)[16] < (Ce,Nd)Fe$_{11}$Ti with 1.73 (2.30)[16] < (Zr,Nd)Fe$_{11}$Ti with 2.69 (3.01) T ([010] to [001]).

The κ values calculated according to Eq. 8 are shown in Tab. 5. The hardness factor (κ) of NdFe$_{11}$Ti, determined using the experimental data of Skokov *et al.*[33], giving a κ of 0.93, which is in good agreement with the calculated κ of 0.77 (0.71 for [100] vs [001]) for LSDA. The κ values calculated with LSDA of RFe$_{11}$Ti (R: Y, Zr, Ce and Nd) show that NdFe$_{11}$Ti has the lowest κ with 0.77 (0.71 for [100] vs [001]). This κ value then increases by 0.27 (0.13 for [100] vs [001]) for ZrFe$_{11}$Ti, followed by

0.41 for YFe$_{11}$Ti and finally by 0.54 for CeFe$_{11}$Ti. In the case of the GGA+U treatment, κ also increases, starting with 0.49 (0.35 for [100] vs [001]) for NdFe$_{11}$Ti, followed by an increase of 0.22 for YFe$_{11}$Ti, 0.54 (0.34 for [100] vs [001]) for ZrFe$_{11}$Ti and finally 0.63 for CeFe$_{11}$Ti. Thus, Zr increases the hardness factor compared to Nd, but to a lesser extent than Y or Ce.

The calculated κ values of the quaternary compound (Zr,Nd)Fe$_{11}$Ti are 0.92 (0.46 for [100] vs [001]) (GGA+U) and 0.97 (0.78 for [100] vs [001]) (LSDA). As there is no direct literature on the Zr compound, it is classified as a semi-hard magnet. Comparing the quaternary compounds (X,Nd)Fe$_{11}$Ti (X: Y, Zr and Ce), (Y,Nd)Fe$_{11}$Ti has the lowest κ values for GGA+U at 0.67, followed by (Ce,Nd)Fe$_{11}$Ti with an increase of 0.16 and (Zr,Nd)Fe$_{11}$Ti with an increase of 0.25. In case of LSDA, (Zr,Nd)Fe$_{11}$Ti has the lowest κ value at 0.97, with the values for (Y,Nd)Fe$_{11}$Ti and (Ce,Nd)Fe$_{11}$Ti being 0.05 higher. Looking at the values according to the easiest perpendicular and easiest in plane direction, Zr has the lowest κ in case of GGA+U and LSDA. In the case of Zr in particular, the GGA+U method gives a more accurate κ than in case of Y or Ce, as can be seen from the differences between the GGA+U and LSDA values. Specifically, the difference is 0.47 for (Y,Nd)Fe$_{11}$Ti, 0.19 for (Ce,Nd)Fe$_{11}$Ti and 0.05 for (Zr,Nd)Fe$_{11}$Ti. The difference of (Zr,Nd)Fe$_{11}$Ti, on the contrary, increases to 0.32 when considering the [100] to [001] values, which is larger than that of the Ce-containing compound.

As in case of K_I and H_a, the substitution of Co reduces κ. For the (Zr,Nd)Fe$_{10}$CoTi compound, the calculated κ values are 0.87 (0.65 for [100] vs [001]) for GGA+U and 0.90 (0.74 for [100] vs [001]) for LSDA. These values are lower than those of the (Zr,Nd)Fe$_{11}$Ti compound, with a decrease of 0.05 (an increase of 0.19 for [100] vs [001]) for GGA+U and a decrease of 0.07 (0.04 for [100] vs [001]) for LSDA. In absence of comparable literature for K_I, H_a and κ for (Zr,Nd)Fe$_{11}$Ti or (Zr,Nd)Fe$_{10}$CoTi, these values can only be approximately compared with the analogue compound (Zr$_{0.3}$Nd$_{0.7}$)(Fe$_{0.75}$Co$_{0.25}$)$_{11.5}$Ti$_{0.5}$. The literature sample gives 1.41 MJ/m^3 for K_I, 1.7 T for H_a and a κ of 0.71.[20] To sum up, the κ values of the quaternary and quinary compounds in this study exceeds those of the referenced literature compounds by following the directions [001] vs [010]. These discrepancies can be attributed to a higher Zr content, as well as higher Ti and lower Co concentrations in the selected compounds. Therefore, a reasonable agreement with the limited available literature can be expected. When the uniaxial anisotropy is ensured by following the directions [001] vs [100], the calculated values show good agreement with the literature.

When comparing the K_I, H_a and κ characteristics between the [001] vs [010] and [001] vs [100] orientations (see Tab. 5 for values), there are noticeable deviations. However, the [001] vs [100] comparison is essential as it ensures the consistency of the MAE values with the uniaxial anisotropy. Regarding K_I, the evaluation shows that NdFe$_{11}$Ti has the closest agreement with the literature in terms of LSDA for [001] vs [010]. In contrast, the comparison of (Zr,Nd)Fe$_{11}$Ti and (Zr,Nd)Fe$_{10}$CoTi with the literature compound (Zr$_{0.3}$Nd$_{0.7}$)(Fe$_{0.75}$Co$_{0.25}$)$_{11.5}$Ti$_{0.5}$ shows a better agreement in case of [001] vs [100]. Nevertheless, the values for

[001] vs [010] remain possible due to the differences between the calculated compounds and the literature compound. Similar observations apply to H_a. Furthermore, the effect of Zr substitution in both properties shows a comparable effect compared to Y and Ce. Regarding κ, all compounds investigated in both contexts are in the range of semi-hard magnets. Furthermore, it is observed that the Zr substitution increases κ towards hard magnets. Consequently, K_1, H_a and κ values of the examined Zr-containing compounds appear promising.

4. Conclusion

Based on positive results for Nd-lean magnets[15,63], we investigated $(Nd,X)Fe_{12-y}Ti_y$ X=Zr compounds for their magnetic properties. Previous results suggested Y and Ce as suitable substitutes.[16] Here, we investigated Zr as an alternative to Nd, as it is more abundant and less expensive.[17,18] Despite the lack of direct experimental data, our theoretical results agree well with the literature on similar compounds. The literature also discusses the effect of Co on phase stability and magnetic properties when substituted with Zr.[11,19,20,63] Our calculations give us confidence in the calculated properties for Nd-lean quaternary and quinary compounds.

An accurate description of the RE-4f electrons is essential for predicting the intrinsic magnetic properties. The highly localized Nd-4f electrons pose a challenge to the accurate calculation of this property using available DFT exchange correlation functionals. To address this, the DFT+U approach with a Hubbard U value of 6 eV was used as a correction scheme, as previously done in literature for 1:12 Nd-based compounds, with favorable results.[15,16,33]

The methodology of our study successfully predicts the overall magnetization trend of 1:12 phases with $NdFe_{11}Ti$ exhibiting the highest magnetization, followed by $ZrNdFe_{11}Ti$ and $ZrFe_{11}Ti$. For $NdFe_{11}Ti$, $\mu_0 M_S$ ranges from 1.38 to 1.70 T, which agrees well with our GGA (GGA+U) calculations of 1.68 (1.69) T. With Zr substitution $\mu_0 M_S$ reaches 1.60 (1.62) T for $ZrNdFe_{11}Ti$ and 1.51 T for $ZrFe_{11}Ti$ using GGA (GGA+U). When compared with $(Zr_{0.3}Nd_{0.7})(Fe_{0.75}Co_{0.25})_{11.5}Ti_{0.5}$, a good agreement can be seen with the experimentally found $\mu_0 M_S$ value of 1.63 T.[63] Our GGA (GGA+U) calculations show a high $|BH|_{max}$ of 510 (525) kJ/m^3 for $ZrNdFe_{11}Ti$, exceeding $Sm_2Co_{17}B$ with 294 kJ/m^3.[75] Notably, $ZrNdFe_{11.5}Ti_{0.5}$, a compound that includes less Ti, has a $|BH|_{max}$ of 600 (603) kJ/m^3 which is smaller than the theoretical $|BH|_{max}$ of $Nd_2Fe_{14}B$ with 688 kJ/m^3.[31] It was also found that the effect of Co on the magnetic properties depends on the presence of Ti in the compound. In combination with Ti, a decrease of the magnetic properties (m_{tot}, $|BH|_{max}$) is observed, while an increase is calculated in the absence of Ti.

The mean field approximation (MFA) computes the Curie temperature, consistently overestimating it in the ferromagnetic (FM) state, but quantitatively in agreement with the existing literature. In particular, $REFe_{11}Ti$ compounds show superior results in the local moment disordered (LMD) state, supported by $NdFe_{12-y}Ti_y$ (y: $0 \leq y \leq 1$) compounds.[82] FM-based calculations tend to overestimate by about 45% for ternary compounds. The calculated Curie temperatures for $(Zr,Nd)Fe_{11}Ti$ are 783 K (FM) and 652 K (LMD), which are higher than the experimental T_C (588 K) for $Nd_2Fe_{14}B$ but lower than the theoretical T_C of 1050 K. A 7.7 at. % Co substitution in $(Zr,Nd)Fe_{11}Ti$ to $(Zr,Nd)Fe_{10}CoTi$ increases T_C by about 85 K.

The magnetocrystalline anisotropy constant K_1 in Nd-based compounds was insufficiently described by generalized gradient approximation (GGA) methods, as reported in previous studies.[16,33,91] The local spin density approximation (LSDA) showed a better agreement with the experimental results. The GGA+U method gave more accurate results with increasing Zr concentration, where Zr (Co) induced an increase (decrease) in magnetocrystalline anisotropy. The hardness factor κ, which indicates a material's potential as a permanent magnet, is derived from K_1 and the saturation magnetization $\mu_0 M_S$. For the 50% Nd-lean $(Zr,Nd)Fe_{11}Ti$ compound a theoretical κ of 0.97 (0.78 in case of [100] vs [001]) has been calculated, classifying it as a semi-hard magnet. To further increase κ, nitrogenation has been proposed, as shown in previous research.[11,16]

In conclusion, this study demonstrates that the substitution of the critical rare-earth (RE) element Nd with the more abundant Zr in $ThMn_{12}$ compounds yields promising RE-lean magnets with magnetic properties comparable to or only slightly inferior to other Nd-lean magnets. Consequently, based on our theoretical calculations, the newly proposed quaternary $(ZrNd)Fe_{24-y}Ti_y$ compounds emerge as potential and promising permanent magnets.

References

1) J. J. Croat, J. F. Herbst, R. W. Lee, F. E. Pinkerton: *J. Appl. Phys.*, **55**, 2078 (1984).
2) M. Sagawa, S. Fujimura, N. Togawa, H. Yamamoto, Y. Matsuura: *J. Appl. Phys.*, **55**, 2083 (1984).
3) D. Bauer, D. Diamond, J. Li, M. McKittrick, D. Sandalow, P. Telleen: (US Department of Energy Office of Policy and International Affairs (PI), 2011), pp. 1–170.
4) M. Pellegrini: 'Report on Critical Raw Materials for the EU', tech. rep. (Ad hoc Working Group, 2014).
5) K. P. Skokov, O. Gutfleisch: *Scr. Mater.*, **154**, 289 (2018).
6) I. Poenaru, A. Lixandru, S. Riegg, B. Fayyazi, A. Taubel, K. Güth, R. Gauß, O. Gutfleisch: *J. Magn. Magn. Mater.*, **478**, 198 (2019).
7) H. Sepehri-Amin, Y. Une, T. Ohkubo, K. Hono, M. Sagawa: *Scr. Mater.*, **65**, 396 (2011).
8) K. Hono, H. Sepehri-Amin: *Scr. Mater.*, **67**, 530 (2012).
9) W. F. Li, T. Ohkubo, T. Akiya, H. Kato, K. Hono: *J. Mater. Res.*, **24**, 413 (2009).
10) H. Sepehri-Amin, T. Ohkubo, S. Nagashima, M. Yano, T. Shoji, A. Kato, T. Schrefl, K. Hono: *Acta Mater.*, **61**, 6622 (2013).
11) N. Sakuma, S. Suzuki, T. Kuno, K. Urushibata, K. Kobayashi, M. Yano, A. Kato, A. Manabe: *AIP Adv.*, **6**, 056023 (2016).
12) D. B. De Mooij, K. H. J. Buschow: *J. Less-Common Met.*, **136**,

207 (1988).

13) K. H. J. Buschow: *J. Magn. Magn. Mater.*, **100**, 79 (1991).

14) A. M. Gabay, G. C. Hadjipanayis: *Scr. Mater.*, **154**, 284 (2018).

15) H. İ. Sözen, T. Klüner: *J. Magn. Magn. Mater.*, **559**, 1 (2022).

16) S. Erdmann, T. Klüner, H. İ. Sözen: *J. Magn. Magn. Mater.*, **572**, 170645 (2023).

17) D. Gielen, M. Lyons: *IRENA*, **48**, 1 (2022).

18) G. M. Mudd: *Sustainability*, **13**, 10855 (2021).

19) K. Kobayashi, S. Suzuki, T. Kuno, K. Urushibata, N. Sakuma, M. Yano, T. Shouji, A. Kato, A. Manabe: *J. Alloys Compd.*, **694**, 914 (2017).

20) S. Suzuki, T. Kuno, K. Urushibata, K. Kobayashi, N. Sakuma, K. Washio, H. Kishimoto, A. Kato, A. Manabe: *AIP Adv.*, **4**, 117131 (2014).

21) S. Fan, F. Wang, Y. Xia, B. Wu, H. D. Qian, Z. Lin, Y. Wang, H. Du, J. Yang, Y. C. Yang: *Mater. Today Phys.*, **35**, 101119 (2023).

22) D. S. Neznakhin, V. E. Maltseva, S. V. Andreev, N. V. Selezneva, E. I. Patrakov, O. A. Golovnia, A. S. Volegov: *J. Magn. Magn. Mater.*, **563**, 169937 (2022).

23) Y. Hirayama, Y. K. Takahashi, S. Hirosawa, K. Hono: *Scr. Mater.*, **95**, 70 (2015).

24) H. Suzuki: *AIP Adv.* **7**, 0 (2017).

25) Y. Hirayama, Y. K. Takahashi, S. Hirosawa, K. Hono: *Scr. Mater.*, **138**, 62 (2017).

26) H. İ. Sözen: *Ab initio phase stabilities of Ce-based hard magnetic materials* (Dr.-Ing. Dissertation, Ruhr-Universität Bochum, 2019).

27) G. Kresse, J. Furthmüller: *Comput. Mater. Sci.*, **6**, 15 (1996).

28) G. Kresse, J. Furthmüller: *Phys. Rev. B*, **54**, 11169 (1996).

29) J. P. Perdew, K. Burke, M. Ernzerhof: *Phys. Rev. Lett.*, **77**, 3865 (1996).

30) S. H. Vosko, L. Wilk, M. Nusair: *Can. J. Phys.*, **58**, 1200 (1980).

31) Y. Tatetsu, Y. Harashima, T. Miyake, Y. Gohda: *Phys. Rev. Materials*, **2**, 074410 (2018).

32) S. L. Dudarev, G. A. Botton, S. Y. Savrasov, C. J. Humphreys, A. P. Sutton: *Phys. Rev. B*, **57**, 1505 (1998).

33) H. C. Herper, K. Skokov, S. Ener, P. Thunström, L. V. B. Diop, O. Gutfleisch, O. Eriksson: *Acta Mater.*, **242**, 118473 (2022).

34) J. Jensen, A. R. Mackintosh: *Rare Earth Magnetism: Structures and Excitations* (Clarendon Press, Oxford, 1991).

35) A. I. Lichtenstein, M. I. Katsnelson, V. P. Antropv, V. A. Gubanov: *J. Magn. Magn. Mater.*, **67**, 65 (1987).

36) J. Korringa: *Physica*, 392 (1947).

37) W. Kohn, N. Rostoker: *Phys. Rev.*, **94**, 1111 (1954).

38) H. Akai: http://kkr.issp.u-tokyo.ac.jp/.

39) H. Shiba: *Prog. Theor. Phys.*, **46**, 77 (1971).

40) H. Akai: *Physica B+C*, **86-88**, 539 (1977).

41) V. L. Moruzzi, J. F. Janak, A. R. Williams: *Calculated Electronic Properties of Metals* (Pergamon Press, New York, 1978).

42) P. Hohenberg, W. Kohn: *Phys. Rev.*, **136**, B864 (1964).

43) W. Kohn, L. J. Sham: *Phys. Rev.*, **140**, A1133 (1965).

44) M. Richter: *J. Phys. D: Appl. Phys.*, **31**, 1017 (1998).

45) N. Drebov, A. Martinez-Limia, L. Kunz, A. Gola, T. Shigematsu, T. Eckl, P. Gimbsch, C. Elsässer: *New J. Phys.*, **15**, 125023 (2013).

46) W. Körner, G. Krugel, C. Elsässer: *Sci. Rep.*, **6**, 24686 (2016).

47) I. Dirba, Y. Harashima, H. Sepehri-Amin, T. Ohkubo, T. Miyake, S. Hirosawa, K. Hono: *J. Alloys Compd.*, **813**, 152224 (2020).

48) H. L. Zang, S. Lu, M. P. J. Punkkinen, Q. M. Hu, B. Johansson, L. Vitos: *Phys. Rev. B*, **82**, 132409 (2010).

49) A. Díaz-Ortiz, R. Drautz, M. Fähnle, H. Dosch, J. M. Sanchez: *Phys. Rev. B*, **73**, 224208 (2006).

50) H. Fujihisa, K. Takemura: *Phys. Rev. B*, **54**, 5 (1996).

51) J. Zhang, Y. Zhao, R. S. Hixson, G. T. Gray, L. Wang, W. Utsumi, S. Hiroyuki, H. Takanori: *Phys. Rev. B*, **78**, 054119 (2008).

52) W. M. Lomer, W. Marshall: *Philos. Mag.: A Journal of Theoretical Experimental and Applied Physics*, **3**, 185 (1958).

53) Y. Zou, M. Li, L. Deng, H. Zhang, X. Guo, L. Li, S. Wu, T. Huang, H. Li, X. Cai, H. Zhuo, S. Ruan, C. Zhou, B. Li: *Mech. Mater.*, **155**, 103776 (2021).

54) J. M. Lock: *Philos. Mag.: A Journal of Theoretical Experimental and Applied Physics*, **2**, 726 (1957).

55) Y. Zhao, J. Zhang, C. Pantea, J. Qian, L. L. Daemen, P. A. Rigg, R. S. Hixon, G. T. Gray, Y. Yang, L. Wang, Y. Wang, T. Uchida: *Phys. Rev. B*, **71**, 184119 (2005).

56) H. C. Jones, A. G. Montgomery, I. B. Lin, J. W. Lue, H. Nadler, R. R. Hake: *Phys. Rev. B*, **16**, 1177 (1977).

57) M. Kołodziej, Z. Śniadecki: *Appl. Sci.*, **13**, 1966 (2023).

58) H. I. Sözen, S. Ener, F. Maccari, K. P. Skokov, O. Gutfleisch, F. Körmann, J. Neugebauer, T. Hickel: *Phys. Rev. Materials*, **3**, 084407 (2019).

59) H. S. Li, J. M. D. Coey: *Handb. Magn. Mater.*, **28**, 87 (2019).

60) M. Akayama, H. Fujii, K. Yamamoto, K. Tatami: *J. Magn. Magn. Mater.*, **130**, 99 (1994).

61) O. Isnard: *Role of interstitial elements on permanent magnet alloys based on rare earth elements and iron: Synthesis, structural study, spectroscopic analysis in relation to magnetic properties* (Ph.D. thesis, University Grenoble, 1993).

62) H. İ. Sözen, S. Ener, F. Maccari, B. Fayyazi, O. Gutfleisch, J. Neugebauer, T. Hickel: *Phys. Rev. Materials*, **7**, 014410 (2023).

63) S. Suzuki, T. Kuno, K. Urushibata, K. Kobayashi, N. Sakuma, K. Washio, M. Yano, A. Kato, A. Manabe: *J. Magn. Magn. Mater.*, **401**, 259 (2016).

64) Y. Harashima, K. Terakura, H. Kino, S. Ishibashi, T. Miyake: *JPS Conf. Proc.*, **5**, 011021 (2015).

65) Y. Hirayama, T. Miyake, K. Hono: *JOM*, **67**, 1344 (2015).

66) Y. C. Yang, X. D. Zhang, S. L. Ge, Q. Pan, L. S. Kong, H. Li, J. L. Yang, B. S. Zhang, Y. F. Ding, C. T. Ye: *J. Appl. Phys.*, **70**, 6001 (1991).

67) C. Piquer, F. Grandjean, O. Isnard, V. Pop, G. J. Long: *J. Appl. Phys.*, **95**, 6308 (2004).

68) T. Fukazawa, Y. Harashima, Z. Hou, T. Miyake: *Phys. Rev. Materials*, **3**, 053807 (2019).

69) A. Vishina, O. Eriksson, O. Y. Vekilova, A. Bergman, H. C. Herper: *J. Alloys Compd.*, **888**, 161521 (2021).

70) T. Fukazawa, H. Akai, Y. Harashima, T. Miyake: *Acta Mater.*, **226**, 117597 (2022).

71) Y. Harashima, K. Terakura, H. Kino, S. Ishibashi, T. Miyake: *Phys. Rev. B*, **92**, 184426 (2015).

72) L. H. Lewis, F. Jiménez-Villacorta: *Metall. Mater. Trans. A*, **44**, 2 (2013).

73) M. J. Dośpiał: *Mater.*, **14**, 2849 (2021).

74) R. Skomski: *Simple Models of Magnetism* (Oxford University Press, 2008).

75) J. M. D. Coey: *IEEE Trans. Magn.*, **47**, 4671 (2011).

76) H. C. Herper, K. P. Skokov, S. Ener, P. Thunström, L. V. B. Diop, O. Gutfleisch, O. Eriksson: *Acta Mater.*, **242**, 118473 (2023).

77) J. Fidler, T. Schrefl, S. Hoefinger, M. Hajduga: *J. Phys.: Condens. Matter*, **16**, S455 (2004).

78) B. L. Gyorffy, A. J. Pindor, J. Staunton, G. M. Stocks, H. Winter: *J. Phys. F: Met. Phys.*, **15**, 1337 (1985).

79) H. Akai, P. H. Dederichs: *Phys. Rev. B*, **47**, 8739 (1993).

80) H. İ. Sözen, E. Mendive-Tapia, T. Hickel, J. Neugebauer: *Phys. Rev. Materials*, **6**, 023603 (2022).

81) H. İ. Sözen: *Comput. Mater. Sci.*, **214**, 111712 (2022).

82) T. Miyake, Y. Harashima, T. Fukazawa, H. Akai: *Sci. Technol. Adv. Mater.*, **22**, 543 (2021).

83) A. M. Schönhöbel, R. Madugundo, C. Echevarria-Bonet, L. E. Zamora, J. M. Barandiarán, G. C. Hadjipanayis: *J. Alloys Compd.*, **946**, 169267 (2023).

84) T. Fukazawa, H. Akai, Y. Harashima, T. Miyake: *IEEE Trans. Magn.*, **55**, 1 (2019).
85) M. Gjoka, C. Sarafidis, G. Giannopoulos, D. Niarchos, G. Hadjipanayis, J. A. Tabares, G. A. Pérez Alcázar, L. E. Zamora: *J. Rare Earths*, **37**, 1096 (2019).
86) C. B. Rong, H. W. Zhang, R. J. Chen, B. G. Shen, S. L. He: *J. Appl. Phys.*, **100**, 123913 (2006).
87) M. Springford, D. Shoenberg: *Electrons at the Fermi Surface* (Cambridge University Press, Cambridge U.K., 1980).
88) S. A. Nikitin, I. S. Tereshina, V. N. Verbetskii, A. A. Salamova: *Phys. Solid State*, **40**, 258 (1998).
89) R. Skomski, J. M. D. Coey: *Scr. Mater.*, **112**, 3 (2016).
90) W. Bouzidi, T. Bartoli, R. Sedek, A. Bouzidi, J. Moscovici, L. Bessais: *J. Mater. Sci. Mater. Electron.*, **32**, 10579 (2021).
91) L. Ke, D. D. Johnson: *Phys. Rev. B*, **94**, 1 (2016).

<Paper>

Characterization of Magnetostrictive Film on Shaft Surface in Inverse Magnetostrictive Torque Sensor Using Magneto-optical Kerr Effect

K. Ishibashi*,**, M. Sonehara**, T. Kodaira*, T. Sasaki*, and T. Sato**

*Sensortronics Laboratory, Tamagawa Seiki Co., Ltd., *1020 Kega, Iida-shi, Nagano-ken, 395-8520, Japan*
** Faculty of Engineering, Shinshu University, *4-17-1 Wakasato, Nagano-shi, Nagano-ken, 380-8553, Japan*

Methods for evaluating the characteristics of magnetostrictive materials include dynamic magnetic domain observation using a magneto-optical Kerr effect microscope, obtaining B-H curves using a vibrating sample type magnetometer that vibrates a magnetized sample with a DC magnetic field, and so on. Generally, magnetic domains are observed in magnetic materials on flat surfaces. The authors previously researched and developed an inverse magnetostrictive torque sensor in which a magnetostrictive material is deposited on a cylindrical shaft surface. Therefore, to accurately evaluate the characteristics of a torque sensor, it is necessary to observe the magnetic domains while torque is applied on a curved surface. This paper explains that method and presents the results of dynamic domain observation of magnetostrictive materials on the shaft surface using a newly developed magneto-optical Kerr effect microscope.

Keywords: magneto-optical Kerr effect, magnetostrictive torque sensor, magnetic domain observation

1. Introduction

Currently, in response to global energy challenges such as mitigating global warming, the automotive industry is accelerating the adoption of next-generation vehicles like electric vehicles (EV) and plug-in hybrid vehicles (PHV) [1]. Moreover, the electrification trend extends to various sectors including robotics, household appliances, drones, and even aircraft. While these initiatives primarily target energy conservation and CO_2 reduction, optimizing the efficiency of electric motors is paramount.

Traditionally, motor control relies on detecting the motor's rotational axis angle and regulating the optimal current flow for each angle [2]. The precision of angle sensors [3,4,5,6] and current sensors [7], which detect the rotational position of the shaft [8], significantly influences motor controllability. However, when the motor transfers power to the shaft, various disturbance load torques such as friction, torsion, and gear effects are generated, limiting control accuracy with conventional angle and current sensors. Therefore, achieving high-efficiency motor control requires the detection and feedback of actual shaft torque, inclusive of disturbances [9]. This paper focuses on an inverse magnetostrictive torque sensor [10,11,12,13] utilizing the inverse magnetostrictive effect [14,15], deemed suitable for motor control. The verification results of an evaluation method for magnetostrictive material films, crucial in determining torque sensor performance, are presented.

Figure 1 (a) illustrates the configuration of the inverse magnetostrictive torque sensor employed in this paper. In the case of an inverse magnetostrictive torque sensor, a magnetostrictive material film is deposited on the surface of the shaft. When torque is applied to the shaft, both tensile and compressive stresses are induced on the magnetostrictive film adhered to the shaft's surface. A winding coil is positioned on the magnetostrictive film as a detection unit to monitor changes in the characteristics of the magnetostrictive material [16]. As torque is applied, both tensile and compressive stresses are exerted on the magnetostrictive material, resulting in alterations of its magnetic properties (permeability) in each direction.
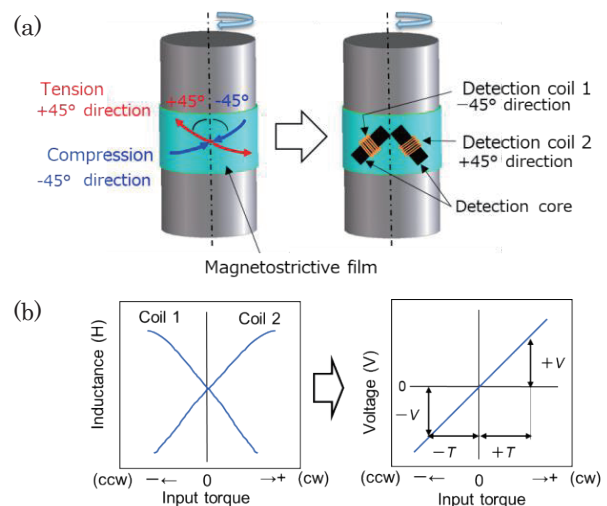

Fig. 1 Principle of inverse magnetostrictive torque sensor detection. (a) Relationship between stress direction and magnetization direction of inverse magnetostrictive torque sensor. (b) Coil inductances change and output voltage characteristics.

Corresponding author: K. Ishibashi (e-mail: kazuyuki-ishibashi@tamagawa-seiki.co.jp).

Therefore, by arranging two coils (detection coil 1 and coil 2) according to the direction of stress, changes in the magnetic properties of the magnetostrictive material can be detected as variations in coil inductance, as shown in Figure 1 (b). By converting this difference into voltage, it is possible to detect the direction and magnitude of applied torque. Note that Figure 1 (b) illustrates the principle and is not based on actual measurement data.

The authors have previously conducted evaluations of sensor characteristics using electroplating as the magnetostrictive film of the magnetostrictive torque sensor[17]. Through this experience, they have recognized the importance of the change in magnetic properties of the magnetostrictive film when torque is applied, as a crucial characteristic of torque sensors. However, at present, a method for properly evaluating the magnetostrictive material formed on the surface of the torque sensor shaft has not been established. The magnetostrictive film material used as a torque sensor needs to be evaluated non-destructively, reproducing the direction of the magnetic field and the state of torque application on the curved surface of the axis to match the shape of the torque sensor. However, conventional magnetic property evaluation methods such as B-H analyzers are not configured to obtain magnetic properties when torque is applied to the magnetostrictive material on the axial surface. This paper focuses on magneto-optical Kerr effect microscopy, which has the advantage of confirming magnetic properties non-destructively. The authors conducted observations of the movement of magnetic domain walls[18] and the observation of magnetic domains according to the operating conditions of the torque sensor, dynamically evaluating the magnetic properties of the magnetostrictive film material[19].

2. Experimental Method

2.1 Experimental device structure

Figure 2 (a) depicts the configuration of the magneto-optical Kerr effect microscope utilized in this study. This apparatus is equipped with a mechanism to exert external torque on the shaft designated for the torque sensor and allows for arbitrary adjustment of the external magnetic field angle. Figure 2 (b) illustrates the configuration of the magneto-optical Kerr effect microscope (NEOARK CORPORATION: BH-753-TSC) employed for shaft evaluation in this research. Table 1 outlines the device specifications. The magnetic field applied during magnetic domain observation ranges from ±24 kA/m (±300 Oe), and due to equipment limitations, only positive torque can be applied to the shaft, with a maximum of 100 Nm.

2.2 Sample shaft overview

Figure 3 illustrates a sample for magnetic domain observation. This sample is a thin-film magnetostrictive sample[20,21] (Fe-Si-B Amorphous Metal Ribbon

Material[22]: Hitachi Metals Metaglas ® 2605SA1, Thickness: 0.025 mm), chosen for its high permeability and low hysteresis characteristics suitable for torque sensing applications. The thin film was affixed to a 40-mm stainless steel shaft using adhesive. With this setup, magnetic domain observation was conducted, and the magnetization curve was determined based on the contrast ratio of the magnetic domain image for each applied torque.
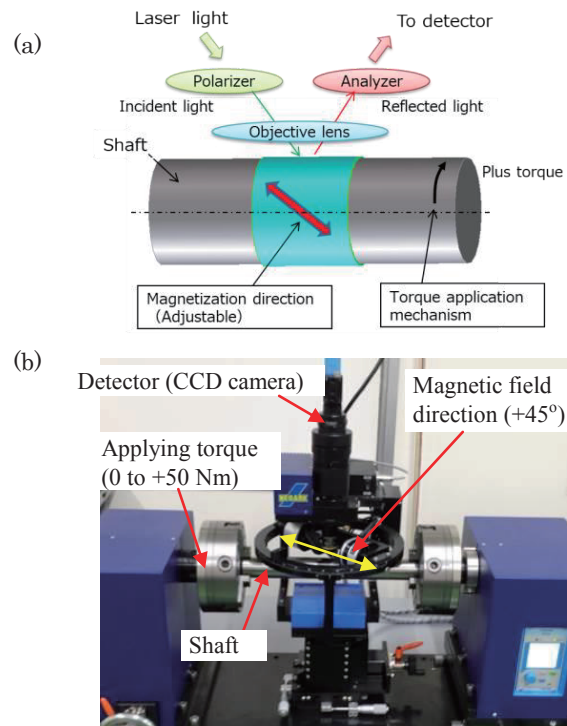

Fig. 2 Overview of Kerr effect microscope. (a) Device function overview. (b) Magneto-optical Kerr effect photomicrograph for shaft evaluation.

Table 1 Kerr effect microscope specifications.

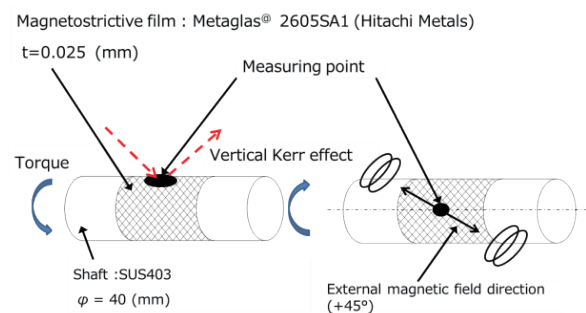| Item	Specification
Observation camera	Number of pixels: 1280×960 Gradation: 12 bit
Objective lens	10 times
Field of view size	480×360 μm
Max magnetic field	±23,873 A/m (±300 Oe)
Max torque	+100 Nm

Fig. 3 Sample shaft overview.

3. Experimental Results

3.1 Magnetic domain image observation results

The direction of the magnetic field applied to the shaft is +45°. Magnetic domain images were observed with applied torques of 0 Nm, 10 Nm, and 20 Nm. Figures 4, 5, and 6 show images for each applied magnetic field and torque. When torque is applied, the surface of the magnetostrictive film in the +45° magnetic field application direction experiences compression. The boundary between contrast shades in the magnetic domain image represents the domain wall, and it is evident that the domain wall moves with each applied magnetic field. In Figures 4, 5, and 6, the applied magnetic field around 400 A/m to 700 A/m, where the movement of the domain wall (change in contrast) is most pronounced, is highlighted. Furthermore, since the applied magnetic field cannot be arbitrarily set due to device resolution, the applied magnetic fields under each condition are not uniform.

3.2 Magnetization curve comparison and consideration

Figure 7 illustrates a graph measuring the magnetization curve from the contrast ratio of the magnetic domain images. The vertical axis represents the contrast ratio, indicating the ratio of gradation when the contrast around ±1000 A/m at 0 Nm is set to ±1. The slope of the magnetization curve represents the magnetic permeability, and in this experiment, the slope becomes gentler at +10 Nm and +20 Nm, resulting in a decrease in magnetic permeability.

1). +667 A/m 2). +621 A/m

3). +552 A/m 4). +489A/m

Domain wall

5). +428 A/m 6). +393 A/m
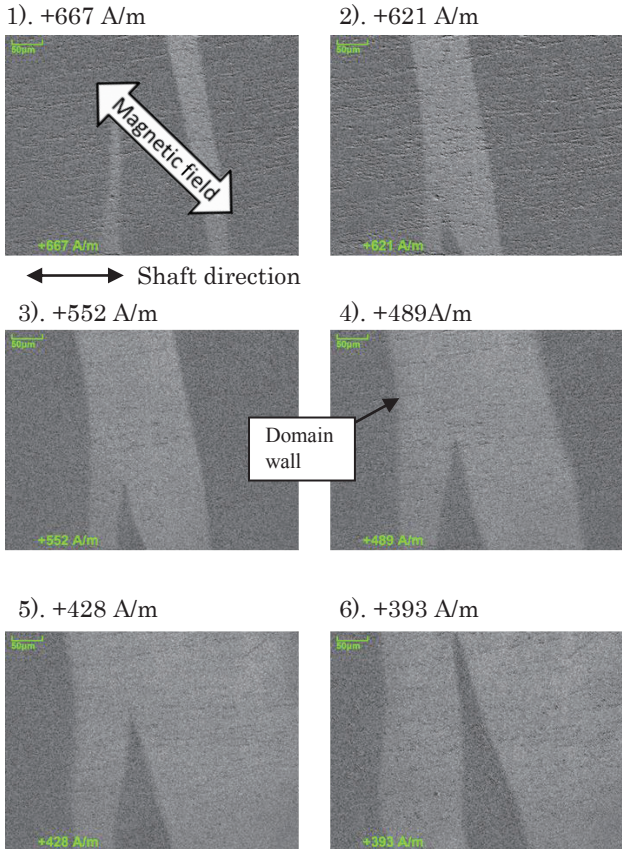
Fig. 4 Magnetic domain image with zero torque.

1). +665 A/m 2). +602 A/m

Magnetic field
+10 Nm Torque
Shaft direction

3). +539 A/m 4). +455 A/m

5). +390 A/m 6). +408 A/m
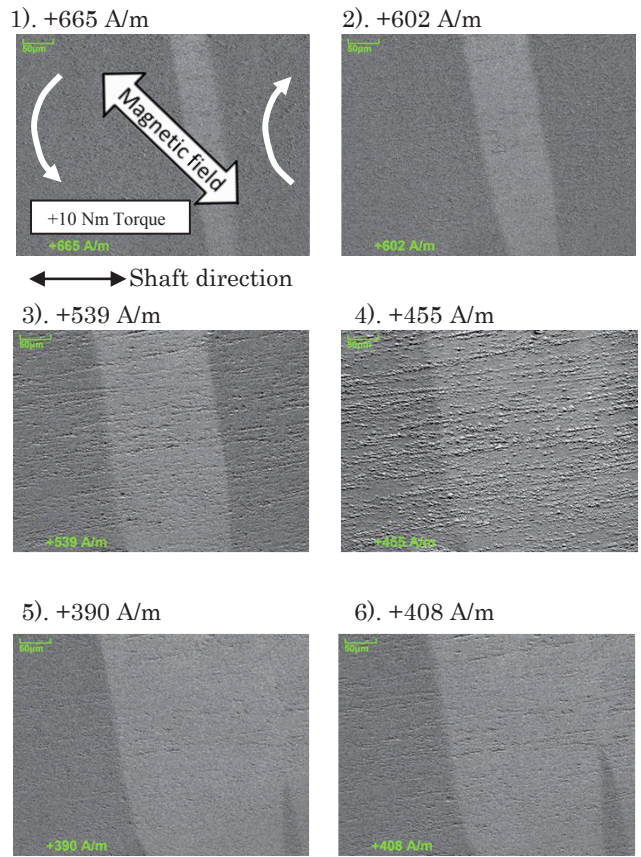
Fig. 5 Magnetic domain image with +10 Nm torque.

1). +657 A/m 2). +602 A/m

Magnetic field
+20 Nm Torque
Shaft direction

3). +528 A/m 4). +467 A/m

5). +429 A/m 6). +377 A/m
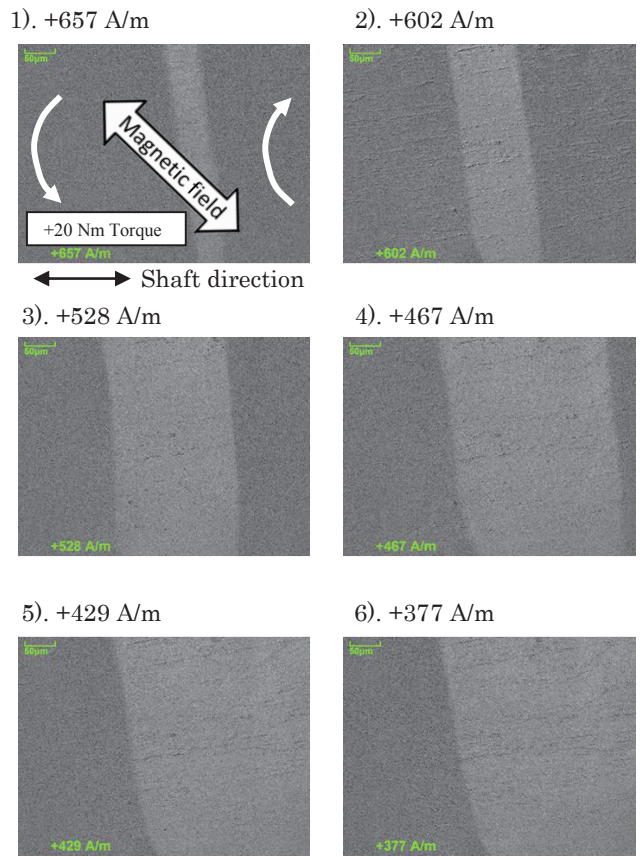
Fig. 6 Magnetic domain image with +20 Nm torque.

Figure 7 (b) is a graph showing the variation in contrast ratio from 400 A/m to 700 A/m within the graph of Figure 7 (a), where the change is notable. Additionally, in Figure 7 (c), the rate of change of the slope of the magnetization curve for each applied torque is depicted. This graph confirms the reproducibility of the applied torque direction, in the sequence of 0 Nm, 10 Nm, 20 Nm, 10 Nm, and 0 Nm. In Figure 7 (c), as the torque increases, the rate of change of the slope of the magnetization curve decreases, and when the torque returns to 0 Nm, the slope reverts to its original value. Magnetic demagnetization is performed for each measurement, hence magnetic hysteresis due to torque application is not considered. Additionally, the contrast ratio at 0 Nm serves as the reference point, set at 100%. The reason for the variation in the slope of the magnetization curve upon applying torque is believed to stem from the phenomenon where the applied torque compresses the magnetostrictive material in the direction perpendicular to the external magnetic field, leading to a decrease in permeability as torque is applied.
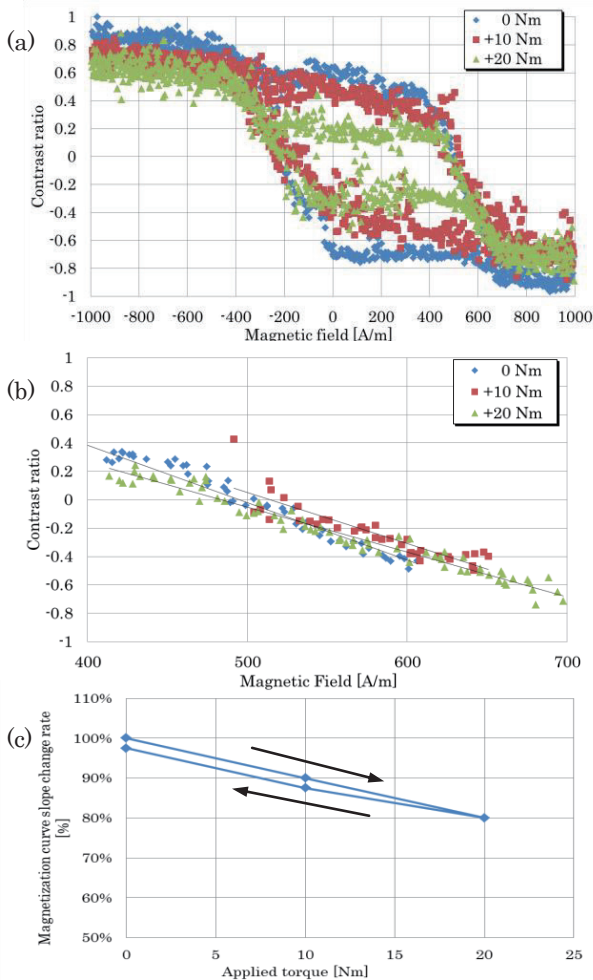
Fig. 7 Magnetization curve for each applied torque. (a) Magnetization curve measured from contrast ratio. (b) Enlarged graph around 400 A/m to 700 A/m. (c) Magnetization curve slope change rate comparison. The arrows indicate the sequence for torque application.

Next, using the same evaluation axis, the slope change of the magnetization curve due to the contrast ratio of the magnetic domain image was confirmed at multiple points. Figure 8 shows the measurement points of the shaft. Four locations were extracted at 90-degree intervals with respect to the axis rotation direction, and magnetic domain images were observed with a magneto-optical Kerr effect microscope for each applied torque. Figure 9 shows a plot of the rate of change in the slope of the magnetization curve for each applied torque at each point. At any point on the axis, the slope of the graph became gentle when +50 Nm torque was applied. At each observation point, the rate of change in the slope of the 0-degree point is approximately ±10%, while at the 90-degree point, it is about ±40%, resulting in an average rate of change of approximately ±20%. The differences observed at each observation point are thought to be due to the non-uniformity in the magnetic properties of the amorphous ribbon foil. Therefore, it is considered possible to improve the accuracy of the torque sensor by arranging multiple detection units and averaging the acquired characteristic results when constructing a torque sensor using materials similar to those used in this experiment.

To compare with the experiment using the magneto-optical Kerr effect microscope, Figures 10 and 11 present the results of confirming the change in coil
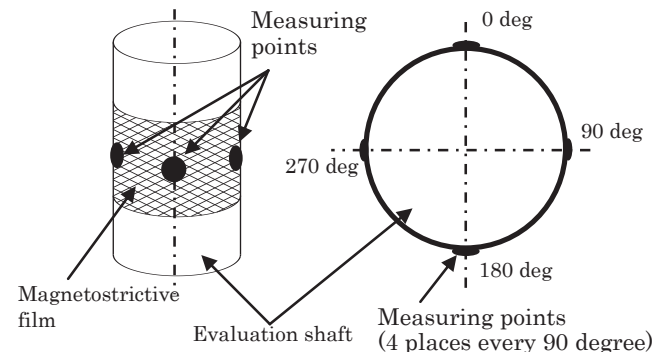

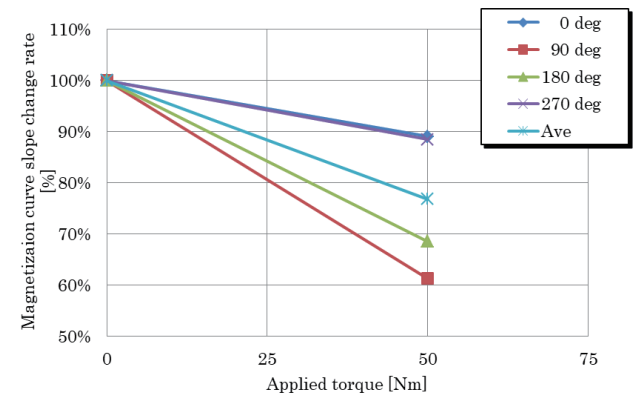Fig. 8 Measurement points on the shaft.

Fig. 9 Magnetization curve slope change rate comparison.

inductance using the same evaluation shaft. Figure 10 depicts the positioning of the detection coil on the evaluation shaft, with the core featuring the detection coil winding oriented at +45° in the axial direction[23]. The core material utilized was permalloy sintered metal, with an air gap of l = 0.1 mm between the core and the shaft. The coil itself consisted of magnet wire with a wire diameter of φ0.1 mm and N = 30 turns. During measurement, the excitation frequency was set to 52 kHz with a current of 10 mA. The coil inductance L at that time can be calculated using the following equation.

$$L = \mu N^2 S/l \quad \cdots (1)$$

In the equation, μ represents the magnetic permeability, and S is the cross-sectional area of the core. Parameters other than μ are fixed values, so L is directly proportional to μ. Therefore, the change in coil inductance L is proportional to the change in μ that occurs when torque is applied to the shaft. Figure 11 illustrates the trend of coil inductance L when torque is applied. At +50 Nm, the surface of the magnetostrictive film of the detection coil oriented at +45° undergoes compression, leading to a decrease in coil inductance L. This indicates a reduction in magnetic permeability μ at +50 Nm. Furthermore, when the torque is returned to 0 Nm, the inductance L reverts to its original value. This trend mirrors the change in the slope of the magnetization curve estimated from the contrast ratio observed with the magneto-optical Kerr effect microscope, as demonstrated in Figure 7 or Figure 9. Additionally, the starting point is set at 100% for 0 Nm. In this scenario, the uppermost point at 0 Nm serves as the starting point.
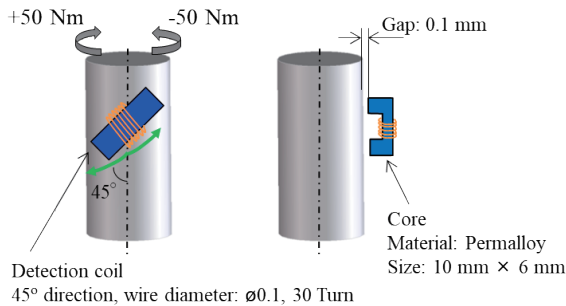
Fig. 10 Detection coil arrangement model.
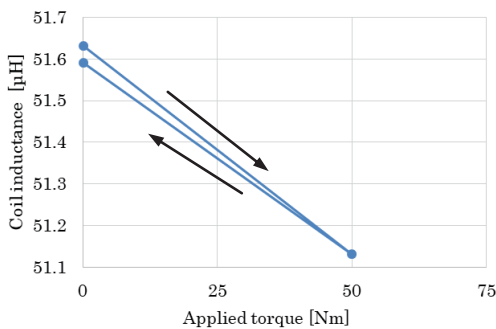
Fig. 11 Graph of coil inductance change rate. The arrows indicate the sequence for torque application.

However, there was a discrepancy in the rate of change between the observed alteration in magnetic permeability using the magneto-optical Kerr effect microscope and the change in magnetic permeability measured via coil inductance. While the magneto-optical Kerr effect microscope measurements showed a change of approximately 10 to 40%, the alteration in coil inductance indicated a result of about 0.3% to 0.4%, significantly diverging from the former. This disparity is attributed to the fact that the external magnetic field generated by the detection coil measurement method is lower than the ±1000 A/m range of the Kerr effect microscope. When calculated with a coil turn number of 30 turns, a current of 10 mA, and a core length of 10 mm, the generated external magnetic field is only about 1/30 of ±30 A/m. Therefore, it is conceivable that the change in magnetic permeability during torque application is minimal.

4. Summary

The trend of the change in the magnetization curve slope measured from the contrast ratio using a magneto-optical Kerr effect microscope for different applied torques was the same as the result of measuring with a coil, but the rate of change itself was different. Moreover, in this evaluation method, a means to quantitatively evaluate permeability has not been established. However, in inductance evaluation using a coil, there are significant error factors such as variations in the coil winding, fluctuations in the magnetic properties of the core, and variations in mounting position. Additionally, increasing the external magnetic field strength, which is the variable in this experiment, requires enlarging the detection unit, thereby imposing limitations on evaluating the material's intrinsic properties. This measurement method, utilizing a magneto-optical Kerr effect microscope, is less susceptible to these factors and is suitable for evaluating the torque sensor shaft in its product state. In the future, by quantifying changes in magnetic permeability, this evaluation method could serve as a benchmark for assessing single-material evaluation methods, contributing to the development of optimal materials for torque sensors.

References

1) Yoshikuni Yoshida, Masashi Kitazato, and Hisashi Ishitani: *J. Adv. Simul. Sci. Eng.,* **6**, 27 (2014).
2) Kiyoshi Sakamoto, Yoshitaka Iwaji, and Tsunehiro Endo: *IEEJ Trans. Ind. Appl.,* **124**, 1133 (2004).
3) K. Masaki, K. Kitazawa, H. Mimura, et al.: *Sens. Actuators, A.,* **81**, 297 (2000).
4) Zahra Nasiri-Gheidari and Farid Tootoonchian: *IEEE Sens. J.,* **15**, 4027 (2015).

5) Zijian Zhang, Fenglei Ni, Yangyang Dong, Chuangqiang Guo, Minghe Jin, and Hong Liu: *IEEE Trans. Ind. Elect.*, **62**, 4408 (2015).

6) T. Masuda and M. Kajitani: *J. Robot. Mechatron.*, **5** , 448 (1993).

7) Naoki Miyamoto and Kiyoshi Ohishi: *IEEJ Trans. Ind. Appl.,* **133**, 627 (2013).

8) Noritaka Aso, Takahiro Tsujimoto, Daisuke Sonoda, and Kazuhiro Shimoda: *Panas. Tech. J.,* **63**, 2 (Nov. 2017).

9) Youichi Hori: *T. IEE Japan.*, **108-D**, 7 (1988).

10) Masashi Mizuno and Katsuhiro Kojima: *Denki-Seiko*, **62**, 167 (1991).

11) Fumitaka Koga Kouji Yoshida, and Ichiro Sasada: *IEEJ Trans. Ind. Appl.*, **117**, 148 (1997).

12) I. Sasada, A, Hiroike, and K. Harada: *IEEE Trans. Magn.*, **20**, 951 (1983).

13) I. Sasada and F. Koga: *J. Appl. Phys.*, **75**, 5916 (1994).

14) Y. Nishibe, Y. Nonomura, K. Tsukada, and M. Takeuchi: *Tech. Dig. Transducers'91.*, 412 (1991)

15) Y. Kubo, S. Hashi, H. Yokoi, K. Arai, and K. Ishiyama: *IEEJ Trans. SM.*, **138**, 4 (2018).

16) Hiroyuki Wakiwaka and Kazunari Banno: *Digests of the 23th Annual Conference on Magnetics in Japan.,* 1429 (1999).

17) Y. Arimura, S. Sueyoshi, N. Mukaibou, M. Doi, and Y. Shimizu: *Int. J. Automot. Eng.*, **50**, 390 (2019).

18) H. J. Williams, F. G. Foster, and E.A. Wood: *Phys. Rev.*, **82**, 119 (1951).

19) Kazuhiro Sugiyama and Kimisuke Shirae: *Digests of the 5th Annual Conference on Magnetics in Japan.,* **22,** B-1 (1981).

20) Yasuyuki Miwa, Jaewon Shin, Yoshiaki Hayashi, et al.: *IEEE Trans. Magn.*, **51**, 1 (2015).

21) Joerg Froemel, Satoru Akita, and Shuji Tanaka: *Micromachines.*, **11**, 649 (2020).

22) Kenji Narita: *J. IEE Japan.*, **98**, 1176 (1978).

23) I. Sasada, F. Koga, and K. Harada: *IEEE Trans Magn.*, **29**, 3186 (1993).

Notice for Photocopying

If you wish to photocopy any work of this publication, you have to get permission from the following organization to which licensing of copyright clearance is delegated by the copyright owner.

〈All users except those in USA〉
Japan Academic Association for Copyright Clearance, Inc. (JAACC)
6–41 Akasaka 9-chome, Minato-ku, Tokyo 107–0052 Japan
Phone 81–3–3475–5618　FAX 81–3–3475–5619　E-mail: info@jaacc.jp

〈Users in USA〉
Copyright Clearance Center, Inc.
222 Rosewood Drive, Danvers, MA01923 USA
Phone 1–978–750–8400　FAX 1–978–646–8600

If CC BY 4.0 license icon is indicated in the paper, the Magnetics Society of Japan allows anyone to reuse the papers published under the Creative Commons Attribution International License (CC BY 4.0).
Link to the Creative Commons license: http://creativecommons.org/licenses/by/4.0/
Legal codes of CC BY 4.0: http://creativecommons.org/licenses/by/4.0/legalcode

複写をされる方へ

当学会は下記協会に複写複製および転載複製に係る権利委託をしています．当該利用をご希望の方は，学術著作権協会（https://www.jaacc.org/）が提供している複製利用許諾システムもしくは転載許諾システムを通じて申請ください．
権利委託先：一般社団法人学術著作権協会
　　　　　〒107-0052 東京都港区赤坂9-6-41　乃木坂ビル
　　　　　電話（03）3475-5618　FAX（03）3475-5619　E-mail: info@jaacc.jp
ただし，クリエイティブ・コモンズ [表示 4.0 国際] (CC BY 4.0)の表示が付されている論文を，そのライセンス条件の範囲内で再利用する場合には，本学会からの許諾を必要としません．
クリエイティブ・コモンズ・ライセンス http://creativecommons.org/licenses/by/4.0/
リーガルコード http://creativecommons.org/licenses/by/4.0/legalcode.ja